

TWISTED SAVONIUS TURBINE BASED MARINE
CURRENT ENERGY CONVERSION SYSTEM

MD. IMTIAJ HASSAN



**TWISTED SAVONIUS TURBINE BASED MARINE CURRENT
ENERGY CONVERSION SYSTEM**

by

© MD. IMTIAJ HASSAN

A Thesis submitted to the
School of Graduate Studies
in partial fulfillment of the requirements for the degree of

MASTER OF ENGINEERING
Department of Electrical and Computer Engineering
Memorial University of Newfoundland
St. John's, Newfoundland

November, 2011

.....To my beloved parents, brother, sister and wife

ACKNOWLEDGEMENTS

During the completion of this research work, I have worked with several personnel whose contributions to this work deserve special mention. It is a great pleasure for me to convey my deepest gratitude to them.

First of all I would like to place my special gratitude to my supervisor Dr. Tariq Iqbal for his valuable advice, guidance and constant support from the very beginning of the research work, to its final stage. His experience in the field of Marine Current technology was invaluable, as he provided me with steadfast encouragement through valuable ideas that helped me to grow as a research student. He gave me the tools I needed to solve the different problems I faced during this research work, and his expertise, foreknowledge, and perception in this field made him a great source for ideas. It is an honor for me to be a student under his supervision.

I would like to record my sincere gratitude to my co supervisor Dr. Michael James Hinchey for his guidance, advice and supervision. He always guided me on the right track in pursuing this degree. His unflinching support and guidance allowed me to complete this work, and it was a pleasure to have him as my co supervisor.

This research work has been supported by the Atlantic Innovation Fund and Seaformatics. I would like to acknowledge them and thank Andrew Cook and all the other members of Seaformatics group. I would also like to show my gratitude to Dr. Vlatimil Masek for his encouragement and appreciation.

I would like to thank Wallace Robert of SeaCraft International Limited, for building the prototype of the twisted Savonius turbine. My special thanks to Brian Pretty for his

support in instrumentation for the experimental set up in the Flume Tank and Wind Tunnel. I learned much from him.

I am indebted to my lab mates and friends who always supported me both directly and indirectly. I am grateful to my friends for their emotional support over this project. My special thanks to one of my very good friends, Md. Nahidul Islam Khan, for his constant support during this time.

During my research work, I always get support from my family members. It is a great pleasure for me that I can acknowledge them. I would like to thank my father Md. Habibur Rahman, my mother Jebun Nassa, my brother Md. Istiak Hassan, my sister Tasnim Tabassum, and the rest of my family members for their endless love and support. My very special thanks to my wife Most. Nusrat Jahan for her perpetual reinforcement.

Table of Contents

ABSTRACT.....	ii
ACKNOWLEDGEMENTS.....	iii
Table of Contents.....	v
List of Tables.....	ix
List of Figures.....	x
List of Symbols.....	xiv
List of Appendices.....	xvii
Chapter 1.....	1
1.1 The ONSFI Project.....	1
1.2 The Seaformatics Pod.....	3
1.3 Thesis Outline.....	5
Chapter 2.....	7
2.1 Introduction.....	7
2.2 Formation of Marine Currents.....	7
2.3 Marine Current Energy Conversion Devices.....	10
2.3.1 Rotating Devices.....	11
2.3.1.1 Types of Marine Current Turbines.....	11
2.3.1.2 Support Structure.....	12
2.3.1.3 Gearbox.....	12

2.3.1.4	Generator	13
2.3.2	Reciprocating Devices.....	13
2.4	Current Status of Marine Current Energy Devices	13
2.5	Technology Challenges.....	20
2.6	Conclusion	21
Chapter 3	22
3.1	Introduction.....	22
3.2	Introduction to CFD.....	23
3.3	CFD vs Experimental Setup.....	25
3.4	Application of CFD	26
3.5	Conservation Laws	27
3.6	Turbulent Hydrodynamics	30
3.7	Volume of Fluid	35
3.8	Moving Bodies in Flow	36
3.9	Conclusion	37
Chapter 4	38
4.1	Introduction.....	38
4.2	Twisted Savonius Turbine	38
4.3	Material Selection.....	45
4.4	Prototype of Twisted Savonius Turbine	47
4.5	Experimental Setup in Flume Tank.....	48
4.5.1	Test Results in Flume Tank	52

4.6	Wind Tunnel Test of the Twisted Savonius Turbine.....	56
4.6.1	Test Results at Wind Tunnel.....	59
4.7	Conclusion	61
Chapter 5.....		62
5.1	Introduction.....	62
5.2	Computational Fluid Dynamics and Flow-3D	62
5.3	Flow 3D Simulation Results	64
5.3.1	Simulation Results of Twisted Savonius Rotor with Overlap Ratio	64
5.3.2	Simulation Results of Twisted Savonius Rotor with a Zero Overlap Ratio	70
5.3.3	Horizontally Mounted Position-1 for the Twisted Savonius Turbine	72
5.3.4	Horizontally Mounted Position-2 for Twisted Savonius Turbine.....	73
5.3.5	Simulation of a Quarter Pitched Savonius Turbine.....	75
5.4	Sensitivity of Mesh.....	77
5.5	Drag Model	78
5.6	Conclusion	80
Chapter 6.....		82
6.1	Introduction.....	82
6.2	The Twisted Savonius Water Current Turbine Emulator	82
6.3	Generator.....	84
6.3.1	Generator Losses	85
6.4	Permanent Magnet Generator	86
6.4.1	Cogging Torque.....	88

6.4.1.1	Starting of a Turbine.....	88
6.4.1.2	Turbine Running Condition.....	89
6.4.2	Reduction of Cogging Torque.....	89
6.5	Twisted Savonius Testing with Generator.....	90
6.6	DC – DC Converters.....	92
6.6.1	Boost Converter.....	96
6.6.2	Design of a Boost Converter.....	98
6.7	Maximum Power Point Tracking Algorithm (MPPT).....	102
6.8	Proposed MPPT Algorithm.....	103
6.8.1	Hardware Setup.....	106
6.8.2	Results.....	107
6.9	Voltage Sensor.....	110
6.10	Current Sensor.....	111
6.11	Energy Storage.....	112
6.12	Conclusion.....	113
Chapter 7	114
7.1	Project Overview.....	114
7.2	Research Contribution.....	115
7.3	Future Work.....	116
Bibliography	118
Appendices	124

List of Tables

Table 3-1 Comparison between CFD and Experimental Set up	26
Table 6-1 Components for building the boost converter	99

List of Figures

Figure 1.1 Marine Current Energy Conversion Systems	2
Figure 1.2 Schematic of Seaformatics	4
Figure 2.1 Thermohaline Circulation [19]	9
Figure 2.2 Spring Tide and Neap Tide	10
Figure 2.3 Seagen [30].....	15
Figure 2.4 Evopod and Free Flow [31,32].....	16
Figure 2.5 Pulse Tidal and Open Centre [33,34].....	17
Figure 2.6 Lunar Tidal Turbine and Tidal Fence Davis Hydro [35,36]	18
Figure 2.7 Neptune Tidal and Stingray Tidal [37,38]	18
Figure 2.8 Gorlov Helical Turbine and Nereus and Solon [39,40]	19
Figure 3.1 CFD Workflow	24
Figure 3.2 2-D Grid	34
Figure 3.3 F Value in CFD Grid.....	36
Figure 3.4 Pressure in a triangular bubble	37
Figure 4.1 Conventional Savonius Turbine (Three Dimensional CAD View).....	40
Figure 4.2 Twisted Savonius Turbine (Three Dimensional CAD View)	40
Figure 4.3 a) Left View (b) Top View (removing the end plate) of Twisted Savonius Turbine.....	41
Figure 4.4 Power coefficient vs TSR Curve of Different Types of Turbines [48]	42
Figure 4.5 Top View of Twisted Savonius Rotor	44
Figure 4.6 Twisted Savonius with Ribs	46

Figure 4.7 Prototype of the Twisted Savonius Turbine.....	47
Figure 4.8 Testing of Twisted Savonius in Flume Tank	49
Figure 4.9 Rotary Encoder	50
Figure 4.10 Experimental Setup for Twisted Savonius	51
Figure 4.11 RPM at Different Current Speeds.....	52
Figure 4.12 Maximum Power Output at Different Current Speeds	53
Figure 4.13 Maximum Power at Different RPM.....	53
Figure 4.14 Turbine Output vs Current Speed Curve.....	54
Figure 4.15 Turbine Torque vs Current Speed Curve	54
Figure 4.16 Cp- λ Curve at Different Current Speed	55
Figure 4.17 Cp- λ Curve of the Twisted Savonius	56
Figure 4.18 The Twisted Savonius in the Wind Tunnel.....	57
Figure 4.19 Torque Arm used in Wind Tunnel Testing	58
Figure 4.20 Instrumentation in the Wind Tunnel.....	59
Figure 4.21 Cp- λ Curve of the Twisted Turbine at Wind Speed of 10 m/s.....	60
Figure 4.22 Cp- λ Curve of the twisted turbine at wind speed of 13 m/s.....	60
Figure 5.1 Twisted Savonius Rotor	64
Figure 5.2 Cross Sectional View of the Mesh Block	65
Figure 5.3 Time Frame at 16.8 Second.....	66
Figure 5.4 Time Frame at 17.1 Second.....	66
Figure 5.5 Time Frame at 17.3 Second.....	67
Figure 5.6 Time Frame at 17.5 Second.....	67

Figure 5.7 Angular Speed of the Turbine at $T=0.5$ Nm Torque	68
Figure 5.8 C_p - λ Curve of Twisted Savonius Turbine.....	69
Figure 5.9 Twisted Turbine with Zero Overlap Ratio	70
Figure 5.10 Mesh Slice with Zero Overlap Ratio	70
Figure 5.11 C_p - λ Curve of Twisted Savonius Turbine with Zero Overlap Ratio.....	71
Figure 5.12 Twisted Savonius as a Horizontal Axis Turbine	72
Figure 5.13 Twisted Savonius Turbine with No End Plates.....	73
Figure 5.14 Horizontally Mounted Turbine at Position 2.....	74
Figure 5.15 C_p - λ Curve for Horizontally Positioned	75
Figure 5.16 Quarter Pitch Twisted Savonius Turbine	76
Figure 5.17 C_p - λ Curve of Quarter Pitch Twisted Savonius Turbine	76
Figure 5.18 Angular Speed of the rotor	77
Figure 5.19 Schematic of Basic Savonius.....	78
Figure 5.20 Strip Model of Twisted Savonius	79
Figure 5.21 Strip Model Power	80
Figure 6.1 MCEC Emulator	83
Figure 6.2 Output (a) Voltage and (b) Current of Generator at Different RPM	83
Figure 6.3 Cross Section of a PMG	88
Figure 6.4 Turbine Coupled with Generator in the Wind Tunnel.....	90
Figure 6.5 Wind Speed vs Voltage Output Curve.....	91
Figure 6.6 Wind Speed vs Current Output Curve	91
Figure 6.7 Wind Speed vs Power Output Curve	92

Figure 6.8 Gain vs Duty Ratio Curve for Different Converters.....	95
Figure 6.9 DC-DC Switching Mode Converter System	95
Figure 6.10 Boost Converter	96
Figure 6.11 Waveforms for Boost Converter.....	97
Figure 6.12 Voltage Current Waveforms for Discontinuous Mode Operation.....	98
Figure 6.13 Schematic of Boost Converter.....	99
Figure 6.14 Proposed Boost Converter.....	100
Figure 6.15 Input vs Output Voltage of the Boost Converter	100
Figure 6.16 Input vs Output Current of the Boost Converter	101
Figure 6.17 Input Voltage vs Output Power of the Converter	101
Figure 6.18 Perturbation and Observation Method Control Action	103
Figure 6.19 Flow Chart of MPPT Algorithm.....	105
Figure 6.20 Hardware Setup	106
Figure 6.21 Angular Speed falls to 8 rad/sec.....	107
Figure 6.22 PWM to reduce Angular Speed	108
Figure 6.23 PWM Signal Variation at Optimum Speed	108
Figure 6.24 Angular Speed Stabilizes around the Optimum Speed	109
Figure 6.25 PWM to increase Angular Speed.....	109
Figure 6.26 Voltage Divider Circuit.....	110
Figure 6.27 Current Sensor	111

List of Symbols

ω	Angular Speed
A	Aspect Ratio
$P_{\text{available}}$	Available power in area A_s in water
b	Body force per unit mass
G	Complex function of velocity gradient
ρ	Density of Fluid
D	Diameter
D_f	Diameter of the endplate
μ	Effective viscosity
μ_t	Extra viscosity
σ	Force per unit area at a point on the surface
g	Gravitational Acceleration
H_s	Height of the rotor
k	Intensity of turbulence
μ_l	Laminar viscosity
ϵ	Local dissipation rate
e	Overlap between two buckets
β	Overlap ratio
P	Power captured by the turbine

C_p	Power coefficient
P	Pressure
R_s	Radius
c	Speed of sound in water
A_s	Swept area
U_s	Tip peripheral velocity
λ	Tip Speed Ratio (TSR)
\mathbf{v}	Velocity
U, V, W	Velocity component in x, y, and z direction respectively
F	Volume of Fluid

Electrical Symbols

C	Capacitance
I	Current
D	Duty ratio
η	Efficiency
L	Inductance
t_{off}	OFF period of the switch
t_{on}	ON period of the switch
T	Period of the control signal
P	Power
R	Resistance
V	Voltage

List of Appendices

Appendix A.....	124
Appendix B.....	132
Appendix C.....	159
Appendix D.....	165
Appendix E.....	167

Chapter 1

Introduction

1.1 The ONSFI Project

The Ocean Network Seafloor Instrumentation (ONSFI) Project is a multidisciplinary research and development project that aims to design, fabricate and validate a proof-of-concept seafloor array of wireless marine sensors for use in monitoring seabed processes. It has four R&D streams: marine sensors; power generation; communication networking; and final integration of the systems into a working prototype. This thesis is a part of the power generation unit. The objective of this work is to self power the pods, utilizing a micro marine current energy conversion system. This will eliminate the need for battery replacement, which can be very expensive and cause sensor down time. The proposed marine current energy conversion system consists of a twisted Savonius Turbine, Permanent Magnet Generator (PMG), Rectifier, Power Electronics Converter, and Battery. The concept is based on a twisted Savonius turbine, directly coupled with a permanent magnet generator. The system is intended to be deployed on the seabed; so, simplicity and robustness are the main focus points. The comprehensive design of the system demands less rotating parts in order to have less maintenance and more reliability, because, once the system is deployed offshore, maintenance is both difficult and expensive. The block diagram of the proposed system is given in Figure 1.1.

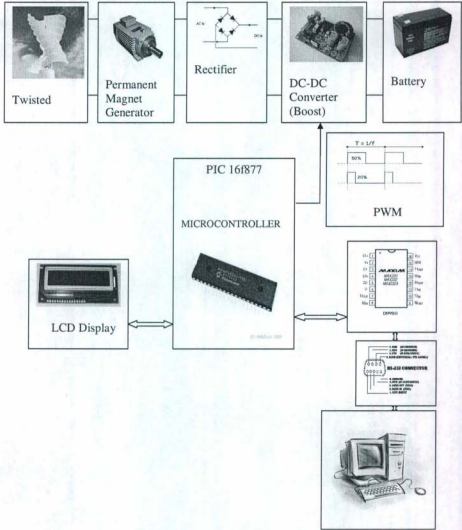


Figure 1.1 Marine Current Energy Conversion Systems

The twisted Savonius rotor converts the marine energy into mechanical energy. At the same time, PMG converts the mechanical energy into electrical energy as it is directly coupled with the rotor. The alternating current (AC) output of the generator is the input of the rectifier. Rectification is the conversion of alternating current (AC) to direct current (DC). This involves a device that only allows one-way flow of electrons. The output of the rectifier is fed to the boost converter, which is a step-up dc-dc switching converter with high efficiency. A low cost microcontroller PIC16f877 based Maximum Power Point Tracking (MPPT) algorithm has been implemented. MPPT tracks the maximum power point by controlling the width of the Pulse Width Modulation which is supplied to the MOSFET (switch). The output of the converter is connected with a battery to store the charges in it. The LCD display connected with the microcontroller displays different data, such as input current, voltage and output voltage, current, and RPM of the turbine shaft. These data are also displayed on the HyperTerminal of a host computer during testing.

1.2 The Seaformatics Pod

A schematic of the Seaformatics pod is shown in Figure 1.2.

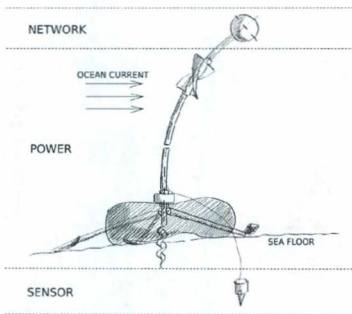


Figure 1.2 Schematic of Seaformatics

According to Project Engineer, Andrew Cook, it is estimated that the target is 100 Watts of power at 1 m/s current speed. This is the target power for this thesis. If this is not reached, scaling laws developed in earlier work [1] will be used to scale the power from this work to that required by the prototype.

1.3 Thesis Outline

This thesis has seven chapters. Concise information about the chapters is given below:

The First chapter gives the total outline of this research work. It discusses the total proposed system in a compact way.

The Second chapter discusses the marine energy sources and current. The marine energy condition is discussed in this chapter in detail along with causes of currents and different types of marine current turbines.

The Third chapter focuses on the theory behind CFD software. It develops the governing Partial Differential Equations or PDEs for turbulent wake flows. It focuses on the discretization of the PDEs and the treatment of moving bodies.

The Fourth chapter shows the experimental set up of the twisted Savonius rotor. The rotor has been tested in the Flume Tank at the Marine Institute and the Wind Tunnel in the Engineering Building at MUN. All the experimental results are presented in this chapter.

The Fifth chapter explores the simulation of the twisted Savonius rotor in the CFD software FLOW-3D. Different simulation results are presented in this chapter. A simple strip power model of the turbine is also developed.

The Sixth chapter provides discussion on the electrical system. This chapter deals with the generator, converter, battery, and MPPT algorithm.

The Seventh chapter presents the conclusions of the research work. It also presents suggestions for future work and research challenges.

Chapter 2

Marine Currents and Energy Conversion Technology

2.1 Introduction

This chapter focuses on the formation of the marine currents. It briefly describes surface and deep water currents and their causes, along with the different parts need to implement a marine current energy conversion system (MCECS). One of the major parts of MCECS is the turbine. This chapter discusses about some marine current turbines in a concise way from commercial view point.

2.2 Formation of Marine Currents

The continuous movement of water in an ocean is called a current. Currents may flow either on or far below the surface of the ocean. They normally move in a specific direction, and aid significantly in the circulation of Earth's moisture, the resultant weather, and water pollution. As seawater is nearly incompressible, vertical movements are associated with regions of convergence and divergence in the horizontal flow patterns. The wind stress acting on the surface layer of the ocean induces movement of that water and causes surface currents. This is called the Ekman Layer transport. In some cases, strong currents are generated because a persistent wind blows in one direction for a long duration [2-11]. The strength and depth of the current depend on the strength and power of the wind. The Coriolis force and the gravity force have significant impact on surface currents. As surface currents travel a long way, the Coriolis force tries to deflect them,

and helps to create a circular pattern [12]. Horizontal currents velocities vary from a few centimeters per second to as much as 4 meters per second. A characteristic surface speed is about 5 to 50 centimeters per second. Currents diminish in intensity with increasing depth.

Other than surface currents, there is also another type of current that is present in deep water. These currents are driven by density differences in water, which in turn depend on the water's temperature and salinity [13,14]. This is also known as Thermo haline circulation (THC). Although this happens mostly due to the density differences, partially there is also a role of gravity for deep water currents. In the case of cold regions, the surface water density is higher than deep water. Pressure gradients at depths resulting from density gradients of the surface water causes circulation [11]. Basically, THC is driven by a push and pull system; in terms of time scale, in the short term it is pushed because of density changes in deep water, and if the density drops too much, then the deep water formation is not possible. But in the long term, it is pulled because of the turbulent mixing of water; deep water density drops until new deep water formations can start. Atlantic warmer surface currents heat up the North Atlantic and Northern Europe. This is shown in Figure 2.1 by the red stream, and the blue stream represents cold North Atlantic deep water. The volume transport of the overturning circulation at the North Atlantic has been estimated from hydrographic section data. It is 17 Sv ($1 \text{ Sv} = 10^6 \text{ m}^3/\text{s}$), with heat transport as 1.2 PW ($1 \text{ PW} = 10^{15} \text{ W}$) [15-21].

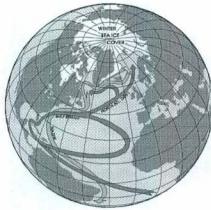


Figure 2.1 Thermohaline Circulation [19]

Energy for turbulent mixing of the water comes from the tides. Tides are the vertical rise and fall of water, and are one of the main factors in ocean current circulation. Tides are generated because of the gravitational attraction forces of the Sun and Moon on the Earth, and the centrifugal force caused by the rotation of Earth on its own axis around the Sun, and the moon's orbit around Earth. The tide rises until it reaches a maximum height, called high tide or high water, and then falls to a minimum level called low tide or low water. Earth rotates on its own axis and the moon rotates around Earth approximately every 24 hours and 50 minutes. At the sub-lunar point, there will be two high tides during the interval. One high tide happens when the moon is overhead, and another high tide occurs 12 hours and 25 minutes later, at the antipode. There will be a low tide between each high tide [22]. When Earth, the moon, and the Sun are in the same line, the Sun and moon's attractive forces act in the same direction. So, the magnitude of the force is higher

than the average value. The tides created for this force are called spring tides. Figure 2.2 shows these tides. While the moon is at the right angle with Earth, and the Sun, the tractive forces of the Sun act on moon's tractive forces at right angle. The resultant force is called neap tides in Figure 2.2. The Neap tides' magnitude is less than the average.

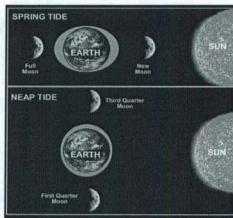


Figure 2.2 Spring Tide and Neap Tide

2.3 Marine Current Energy Conversion Devices

Nowadays, two issues are of major concern in this world: One is that human beings are using limited fossil fuel in at an extensive rate, and secondly, are generating too much waste. Because of these issues, the environmental balance is in danger of disproportion. That is why different systems have been developed to extract clean energy, and new and improved energy methods continue to be developed. Marine current energy conversion

devices are used to harness energy from the ocean. Marine current energy conversion devices may be either rotating or reciprocating [23].

2.3.1 Rotating Devices

Marine current turbines (MCT) are used as rotating devices. A number of blades are connected to the hub, which is called the rotor. Depending upon the axis of rotation, the turbines may be of vertical or horizontal axes.

2.3.1.1 Types of Marine Current Turbines

Hydrodynamic forces generated in the fluid flow act on the MCTs, to move the blades of the turbine that generates electricity. The turbines may be placed on vertical or horizontal axes.

- Horizontal axis marine current turbines – These turbines rotate around the horizontal axis most likely parallel to the current flow. The application scenario determines the number of blades of the turbines. Multi-bladed turbines develop higher starting torque, but the hydrodynamic efficiency is lower. The turbine blade may be of constant or variable pitch. Even different control techniques can be applied to the turbines, depending on the energy requirements and its location [24].

- Vertical axis marine current turbines – These turbines rotate around the vertical axis, and most likely these remain perpendicular to the flow. They also can be multi-bladed. Starting characteristics are an important issue with this turbine. Savonius turbines have a higher starting torque, but Derrius turbines have a lower starting torque. The turbine is mounted on the system, and the generator is connected on the top or down the bottom of the system. This type of turbine can be drag or lift based. Sometimes a vertical axis hybrid type turbine is made with both drag and lift type devices, to satisfy the application requirements [25-27].

2.3.1.2 Support Structure

Support for the turbines is a vital issue for developing such a system. Sometimes the output of the system is influenced by its support structure, and sometimes the system has to experience very harsh environments under the sea, while the current velocity is too high. Gravity Structure, Monopile Structure, Floating Structure, and Tripod Structure are different types of support structure [28].

2.3.1.3 Gearbox

Under the ocean the water speed is low, resulting in a slow turbine rotational speed. Therefore, a gear box is used when the turbine is coupled with a generator. The gear-box converts the high torque and low angular speed of the turbine to low torque and high speed, in order to couple it with the generator. The gear ratio depends on the system design; moreover, the goal is to always use gears with the least amount of friction.

2.3.1.4 Generator

The turbine converts ocean energy to mechanical energy, and this mechanical energy is converted to electrical energy by a generator. Basically, generators can be classified into two groups: Alternating Current Generators and Direct Current Generators. Many of the marine current energy conversion systems use permanent magnet generators.

2.3.2 Reciprocating Devices

Apart from rotating devices, there is another kind of tool called a reciprocating device. Fluid flow creates a hydrodynamic lift force on the hydrofoil of the reciprocating devices, which causes oscillation in them. They produce high torque but low speed. These devices are generally hydraulic power take-off systems utilizing high-pressure oscillating rams. These rams pressurize and transfer the high pressure oil to drive a hydraulic motor, which in turn drives an electric generator. Efficiency is a major issue for this kind of device. If this system is stopped, it takes a long time to make it dynamic again, because lift force is required on the foils [29].

2.4 Current Status of Marine Current Energy Devices

There are some companies working on marine current energy devices. A number of them are commercializing their products, while other products are still under development. Day by day, the popularity of marine current devices is increasing, and Marine Current Energy Devices are taking part to large-scale energy generation.

Seaflow Project: Marine Current Turbine Ltd. is one of the leading companies building marine current turbines. The world's first ever tidal turbine was tested in 1994-5 in the Corran Narrows, Loch Linnhe, Scotland. It could generate 15 kw and had a diameter of 3.5 meters. This turbine is now in the museum of Scotland. The Seaflow project developed the world's first tidal turbine and the most powerful marine renewable energy device in the sea. They did the designing and building of a full scale tidal turbine that could generate 300kw. It was installed 3 km NE of Lynmouth of north Devon coast in May 2003, and decommissioned in October 2009. Recently, they installed a full scale commercial system known as Seagen, in May 2008. Seagen is the largest and most powerful tidal current turbine in the world. Its 16 meter diameter twin rotors sweep over 200 square meters of flow. It can achieve an efficiency of 48% over a broad range of flow velocity. The Seagen is an axial flow pitch controlled rotor. It is operational in Strangford Narrows, Northern Ireland, with a rated power of 1.2 MW at a current velocity of 2.4 m/s. When it experiences a high flow, Seagen's rotor blades can be pitched to limit the power to a pre determined rated power. It can even be pitched 180° , so it can run bidirectional (on the ebb and flood tide). In cases that use a tidal current turbine system, the turbine has to be mounted on a strong structure, because flowing marine currents generally produce huge thrust, typically in the order of 100 tons per MW, showing that the mounting of the turbine is also a very important issue. Seagen is mounted on a structure securely seated on the seabed [30]. Figure 2.3 shows the Seagen.

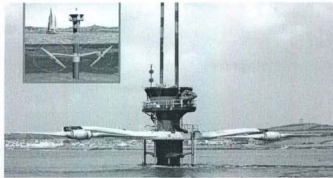


Figure 2.3 Seagen [30]

Evopod: Evopod is a device for generating electricity from free flowing tidal streams, river estuaries, and ocean currents. It is five bladed, having a diameter of 1.5 m, and has a horizontal axis of rotation. A 1/10th scale Evopod (Figure 2.4) and its mooring systems were tested in real tidal stream conditions of Strangford Narrows near Queen's University, at Belfast's Portaferry Marine Laboratory. Testing of the 10th scale unit started in June 2008 and continued into 2009. During 2010, the installation was extended to allow the device to be grid-connected at the Marine Laboratory. A twin-turbine version of its Evopod semi-submerged tethered platform is under development. At full scale, the unit would be fitted with twin 1.2MW rated generators, each coupled to a 16m diameter three-bladed turbine. The unit would generate its combined rated output of 2.4MW in flow speeds of 3.2m/s or above [31].

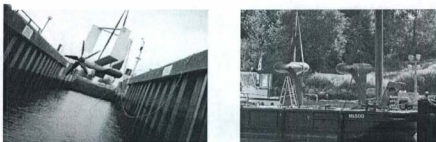


Figure 2.4 Evopod and Free Flow [31,32]

Free Flow System: The Free Flow Kinetic Hydropower System is a horizontal axis turbine with three blades. It has a 4.68m diameter and was developed by Verdant Power Ltd. during 2006 – 2008. Verdant Power successfully demonstrated this technology in a tidal setting through the RITE Project in New York City's East River. Verdant Power Canada will generate clean renewable energy from the natural currents of the St. Lawrence River near Cornwall, Ontario. Ultimately, the project could generate up to 15 MW of power locally. Figure 2.4 shows the free flow turbine [32].

Pulse Tidal: Pulse Generation Ltd. (UK) has developed a reciprocating device (Figure 2.5) that uses a hydraulic generator. The device is currently in the design stage. In April 2008, permission was granted to deploy the prototype in the Humber Estuary in the UK [33].

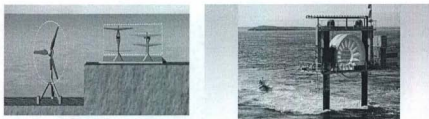


Figure 2.5 Pulse Tidal and Open Centre [33,34]

Open Centre Turbine: This system was developed by Open Hydro Ltd. (Ireland). It has a 6 meter dia and an open centre rotor and stator (Figure 2.5). It has a horizontal axis of rotation and was installed at EMEC off Orkney in Scotland. The turbine was connected to the UK national grid in May 2008 [34].

Lunar Energy Tidal Turbine: Developed by Lunar Energy Ltd. (UK) [35], the design is still under development. The company has agreed to a 500 million Euro deal to install 300 turbines off the coast of Korea. The proposed diameter is 11.5m (Figure 2.6).

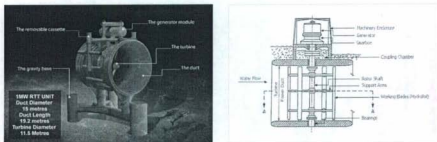


Figure 2.6 Lunar Tidal Turbine and Tidal Fence Davis Hydro [35,36]

Tidal Fence Davis Hydro Turbine: Blue Energy Ltd. (Canada) has developed this turbine (Figure 2.6). Turbines are fixed in an array known as a Tidal Fence. It is a four-bladed design and has a vertical axis of rotation. It is still in the design stage [36].

Neptune Tidal Stream Turbine: This device is now in the design stage. Testing of this device is expected to commence at the EMEC in 2011. It has twin horizontal axes, and three-bladed rotors (Figure 2.7). Aquamarine Power Ltd. (UK) is developing this turbine [37].

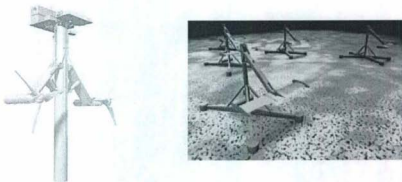


Figure 2.7 Neptune Tidal and Stingray Tidal [37,38]

Stingray Tidal Energy Converter: This is a reciprocating device and utilizes a hydraulic generator (Figure 2.7). A prototype was installed in the Yell sound off the Shetland coast in September 2002, and was removed weeks later. Engineering Business Ltd. developed it [38].

Gorlov Helical Turbine: This turbine is 2.5m in height and 1m in dia. It has a vertical axis of rotation and has twisted blades (Figure 2.8). This device was installed in the Uldolmok Strait off the coast of Korea. It was developed by GCK Technology Ltd. (USA) [39].

Nereus and Solon Tidal Turbine: Nereus's dimension is 12m x 4m and Solon has a diameter of 16m. They both have a horizontal axis of rotation. Nereus is a robust turbine and Solon is a ducted deep water turbine (Figure 2.8). These were developed by Atlantis Resource Corporation PTE Ltd. (Singapore), and were tested in 2008. Solon produced in excess of 500kW in 8 knots of water flow during testing, representing over 50% throat efficiency [40].

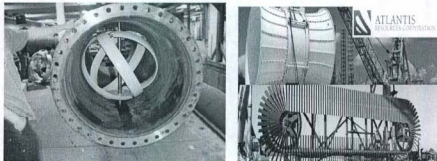


Figure 2.8 Gorlov Helical Turbine and Nereus and Solon [39,40]

2.5 Technology Challenges

There are many more technological challenges in developing a complete marine current energy conversion system:

- First, the main challenge is to synchronize the whole system with the ocean's environment. In depth analysis of resource and device interaction is required to deliver the predicted design performance.
- Turbulence and cavitations effects; the effects of increasing the size of a scaled model and manufacturing methods are some challenging issues for system design.
- There are some complexities to install the system underneath the ocean in a harsh environment, such as foundation or mooring issues, electrical connectors, and submarine cabling.
- The system would be functioning underneath the ocean's surface for a long time. This can be addressed along with the maintenance, biofouling, coating, and sealing.
- The cost of the whole system and the expected output from the system should be balanced.

2.6 Conclusion

Newfoundland and Labrador might be a useful location for marine current turbines. With proper selection of locations and technology, marine energy can be harnessed on a large scale. In this regard, optimization of the energy conversion system is a challenge. The turbine is one of the major devices for MCECS. Worldwide, many companies are commercializing different turbines, using many different concepts to meet the many challenges of MCECS.

Chapter 3

Computational Fluid Dynamics Study

3.1 Introduction

This chapter discusses the theory behind Computational Fluid Dynamics (CFD), beginning with the basic workflow of CFD. Conservation laws are subsequently described, in a comprehensive way. As turbulent wake is a common phenomenon in under ocean flow, a synoptic discussion has been presented in this chapter. Non-linear, transient, second-order differential equations are applied to describe fluid motion. Defining a Mesh is a decisive issue for CFD analysis. CFD does the calculations to find out different unknowns in the grid nodes. Physical space is divided into discrete points, depending on the number of cells in the space. Finer mesh in the space does the calculations in very close points, but it is not always possible to do the simulations with finer mesh, because of time constraints and computer capability. Mesh and numerical solution algorithms can be of different types. Flow-3D has been used as the Computational Fluid Dynamics software package in this work. It works on either finite difference or finite volume algorithms. The Volume of Fluid (VOF) is applied to find the surface of the fluid in Flow-3D. General moving objects will also be examined in this chapter.

3.2 Introduction to CFD

Computational complexity is the main challenge in flow analysis that limits the accuracy of flow-related problems. Turbulence, chemical reactions, heat transfer, mass transfer, and bubbles in the fluid make finding the solutions difficult. Hand calculation of enormous numbers of equations for fluid flow is quite impossible. This is why CFD has been introduced, to solve flow related problems. CFD gives a comprehensive analysis of flow problems through proper selection of computational parameters, grid, and resolution of the grid. It gives realistic results within a very short span of time, satisfying the cost constraints. For a CFD analysis, the whole region of interest is divided into small cells. Depending on the resolution of the grid, the set of differential equations is solved for the flow. Calculations are done in every small place of the regime, and the results are returned to the user interface. Calculations are done discretely. A block diagram of CFD workflow is shown in Figure 3.1.

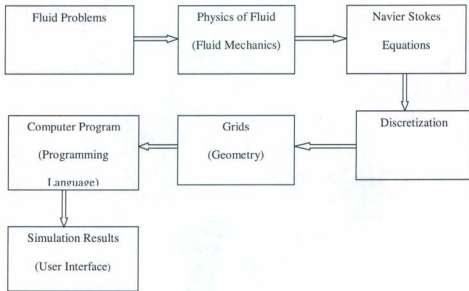


Figure 3.1 CFD Workflow

First of all, the physical properties of the fluid must be recognized from a fluid mechanics point of view for a certain fluid problem. The mathematical equations are written that represent the physical properties of the fluid according to fluid mechanics. These equations are usually a set of partial differential equations. Using them, the Navier-Stokes Equation can be derived, and this is the governing equation of CFD. The Navier-Stokes Equation is analytical; it is understandable and can be solved on a piece of paper. But for a practical application involving a whole regime, numerous equations must be solved to get the CFD solution. Thus, hand calculations are not possible, because of time constraint and calculation complexity; they have to be done using computers. Therefore, these equations must be converted into discretized form. Finite Difference, Finite Element, and

Finite Volume methods are some of the numerical discretization methods used to discretize the equations. The whole problem domain is divided into small grids, or elements, as discretization is based on them. Initial and boundary conditions are very important issues for a fluid problem, and must be defined to get CFD results. Then, the program is written to solve the equations. The typical languages are Fortran and C. The solution method can be either direct or iterative. As CFD analysis requires solution of a large number of differential equations; therefore, workstations or computers with very good configurations are required to run the program. During the simulation, certain control parameters are used to control the convergence, stability, and accuracy of the method. After finishing the simulation, different CFD software represents simulation results in their own way. Some of them give analysis results from different points of view, as well as excellent visualizations of the results [41,42].

3.3 CFD vs Experimental Setup

It is not possible to replace the experimental setup completely by the CFD, because sometimes CFD inputs may involve extensive guessing, and available computer capability may be an issue. But, CFD gives insight into the fluid flows that are too expensive, difficult or sometimes impossible for experimental setups. The table shows the comparison of CFD and Experimental setup.

Table 3-1 Comparison between CFD and Experimental Set up

	CFD	Experimental Setup
Cost	Cheaper	Expensive
Scale	Any	Small/Middle
Optimization Cost	Lesser	More
Information	All	Measured point
Safety	Yes	Sometimes Dangerous

3.4 Application of CFD

CFD has a wide range of applications. It is extensively utilized in industries and research areas. Some areas of CFD application are as follows:

Aerospace	Architecture	Biomedicine
Automotive	Chemical Processing	Civil Engineering
Steel industry	Hydraulics	Power generation
Renewable energy	Turbo machinery	Glass industry
Sports	Marine application	Semiconductor Industry
Water and wastewater	Heat ventilation air condition	

3.5 Conservation Laws

There are often too many groups in the fluid flow to follow. So, the Lagrangian Formulation is not that practical from a mathematical point of view, as it focuses on a specific group of fluid particles. Mathematically, the Eulerian Formulation is much more practical, as it focuses on a specific region of fluid. Using the Transport Theorem it is possible to switch from the Lagrangian Formulation to the Eulerian Formulation. V is an arbitrary specific group of fluid volume and S is the surface anywhere in the flow. dV is a differential volume within V volume having a density of ρ that gives the mass ρdV . \mathbf{v} is the velocity of fluid. U, V , and W are velocity components in x, y , and z direction. \mathbf{v} is represented as:

$$\mathbf{v} = U\mathbf{i} + V\mathbf{j} + W\mathbf{k}$$

According to the Conservation of Mass, the time rate of change of the mass of the group is zero. So,

$$D/Dt \int_{V(t)} \rho dV = 0 \quad (3.1)$$

Using the Transport Theorem this is written

$$\int_{V(t)} [\partial\rho/\partial t + \nabla \cdot (\rho\mathbf{v})] dV = 0 \quad (3.2)$$

According to the Conservation of Mass, the term in the square brackets is zero.

Expanding this term, it can be written

$$\partial\rho/\partial t + \rho\partial U/\partial x + \rho\partial V/\partial y + \rho\partial W/\partial z + U\partial\rho/\partial x + V\partial\rho/\partial y + W\partial\rho/\partial z = 0 \quad (3.3)$$

According to the definition of incompressible fluid, the change of density is zero. So,

$$\partial U/\partial x + \partial V/\partial y + \partial W/\partial z = 0 \quad (3.4)$$

Eq. 3.4 is called the Continuity Equation.

For a differential volume dV , the momentum would be $\rho dV\mathbf{v}$. The time rate of change of the momentum of the group is equal to the net force acting on it, called Conservation of Momentum. So,

$$D/Dt \int_{V(t)} \rho \mathbf{v} dV = \int_{S(t)} \boldsymbol{\sigma} dS + \int_{V(t)} \rho \mathbf{b} dV \quad (3.5)$$

Where $\boldsymbol{\sigma}$ is force per unit area at a point on the surface. Surface forces can be due to pressure and viscous friction. \mathbf{b} is a vector representing the body force per unit mass at any point within the volume. Body forces are basically due to gravity. The Transport Theorem gives

$$\int_{V(t)} [\partial(\rho \mathbf{v})/\partial t + \nabla \cdot (\rho \mathbf{v} \mathbf{v})] dV = \int_{S(t)} \boldsymbol{\sigma} dS + \int_{V(t)} \rho \mathbf{b} dV \quad (3.6)$$

Manipulation gives

$$\int_{V(t)} [X_i + Y_j + Z_k] dV = 0 \quad (3.7)$$

Mathematics requires that

$$X = 0 \quad Y = 0 \quad Z = 0 \quad (3.8)$$

Expansion gives

X momentum

$$\begin{aligned} \rho \partial U/\partial t + \rho (U \partial U/\partial x + V \partial U/\partial y + W \partial U/\partial z) &= - \partial P/\partial x \\ + \partial/\partial x (\lambda [\partial U/\partial x + \partial V/\partial y + \partial W/\partial z]) &+ \partial/\partial x (\mu [\partial U/\partial x + \partial U/\partial x]) \\ + \partial/\partial y (\mu [\partial V/\partial x + \partial U/\partial y]) &+ \partial/\partial z (\mu [\partial W/\partial x + \partial U/\partial z]) \end{aligned} \quad (3.9a)$$

Y momentum

$$\begin{aligned} \rho \partial V / \partial t + \rho (U \partial V / \partial x + V \partial V / \partial y + W \partial V / \partial z) &= -\partial P / \partial y \\ + \partial / \partial y (\lambda [\partial U / \partial x + \partial V / \partial y + \partial W / \partial z]) + \partial / \partial x (\mu [\partial V / \partial x + \partial U / \partial y]) \\ + \partial / \partial y (\mu [\partial V / \partial y + \partial V / \partial y]) + \partial / \partial z (\mu [\partial W / \partial y + \partial V / \partial z]) \end{aligned} \quad (3.9b)$$

Z momentum

$$\begin{aligned} \rho \partial W / \partial t + \rho (U \partial W / \partial x + V \partial W / \partial y + W \partial W / \partial z) &= -\partial P / \partial z - \rho g \\ + \partial / \partial z (\lambda [\partial U / \partial x + \partial V / \partial y + \partial W / \partial z]) + \partial / \partial x (\mu [\partial W / \partial x + \partial U / \partial z]) \\ + \partial / \partial y (\mu [\partial V / \partial z + \partial W / \partial y]) + \partial / \partial z (\mu [\partial W / \partial z + \partial W / \partial z]) \end{aligned} \quad (3.9c)$$

Stokes' hypothesis states $\lambda = 2/3\mu$. A fluid like water is incompressible and has constant viscosity. In this case, Equation 3.9 reduces to

X momentum

$$\begin{aligned} \rho \partial U / \partial t + \rho (U \partial U / \partial x + V \partial U / \partial y + W \partial U / \partial z) &= -\partial P / \partial x \\ + \mu (\partial^2 U / \partial x^2 + \partial^2 U / \partial y^2 + \partial^2 U / \partial z^2) \end{aligned} \quad (3.10a)$$

Y momentum

$$\begin{aligned} \rho \partial V / \partial t + \rho (U \partial V / \partial x + V \partial V / \partial y + W \partial V / \partial z) &= -\partial P / \partial y \\ + \mu (\partial^2 V / \partial x^2 + \partial^2 V / \partial y^2 + \partial^2 V / \partial z^2) \end{aligned} \quad (3.10b)$$

Z momentum

$$\begin{aligned} \rho \partial W / \partial t + \rho (U \partial W / \partial x + V \partial W / \partial y + W \partial W / \partial z) &= -\partial P / \partial z - \rho g \\ + \mu (\partial^2 W / \partial x^2 + \partial^2 W / \partial y^2 + \partial^2 W / \partial z^2) \end{aligned} \quad (3.10c)$$

These are called Navier Stokes equations, which are the basis of most CFD [43].

3.6 Turbulent Hydrodynamics

Fluid particle motion has a laminar or layered structure at low speed. In fluid, particles can move as groups in small spinning bodies. They are called eddies. At high speeds, there is a chaotic or random motion of the eddies. This flow pattern is called turbulent flow. A turbulent wake flow contains lots of small eddies along with some large eddies. Smaller eddies are carried along by the local flow and those are associated with turbulence. But the large eddies remain roughly in place and the fluid in them swirls around and around or recirculates roughly around closed orbits. The smaller eddies remain near to the wake boundaries whereas large eddies remain inside the wakes. Smaller eddies are generated in regions where velocity gradients are high, like at the edges of the wakes or the boundary layers close to the structures. They are dissipated in the region where the velocity gradients are small, such as in sheltered areas like corners. Conservation laws are applicable for turbulent wake flows but they are so complex that analytical solutions are not possible. That's why CFD has been developed based on the conservation laws to serve the purpose. Smaller eddies are so small that they require very fine grids and small time steps to follow the small eddies. Small eddies are 1 mm in dia. So, for CFD it requires a grid spacing less than 0.1 mm to follow the eddies. CFD works on a set of Algebraic Equations (AE) that are converted from the governing equations. Enormous numbers of AEs have to be able to handle to follow the small eddies. So, workable CFD is not possible, because a computer cannot handle the huge number of AEs. For example, if the grid spacing is 0.1 mm, a 100 m X 100 m X 100 m volume of water would need $10^6 \times 10^6 \times 10^6$ or 10^{18} grid points. It also requires small time steps to

do the simulations. But, currently there is no computer that can handle so many grid points with small time steps. The fluid appears more viscous than it is when the small eddies in a turbulent flow diffuse momentum. Models which account for this apparent increase in viscosity are known as eddy viscosity models. This type of model is obtained from momentum equations by a complex time averaging process. The developed model can estimate the variation of eddy viscosity throughout the flow. Now, it is not necessary to follow the small eddies because, according to the modeling, they are already suppressed by eddy viscosity. Considering this, a workable CFD is possible with larger grid spacing and time stepping. However, it requires $10^2 \times 10^2 \times 10^2$ or 10^6 grid points whereas previously it required 10^{18} . Therefore, a workable CFD is only possible with a turbulence model. As well, hydrodynamic flows are often turbulent flows. The governing equations for flow with this model can be written as:

Momentum Equations:

$$\rho \left(\frac{\partial U}{\partial t} + U \frac{\partial U}{\partial x} + V \frac{\partial U}{\partial y} + W \frac{\partial U}{\partial z} \right) + A = - \frac{\partial P}{\partial x} + \left[\frac{\partial}{\partial x} (\mu \frac{\partial U}{\partial x}) + \frac{\partial}{\partial y} (\mu \frac{\partial U}{\partial y}) + \frac{\partial}{\partial z} (\mu \frac{\partial U}{\partial z}) \right] \quad (3.11a)$$

$$\rho \left(\frac{\partial V}{\partial t} + U \frac{\partial V}{\partial x} + V \frac{\partial V}{\partial y} + W \frac{\partial V}{\partial z} \right) + B = - \frac{\partial P}{\partial y} + \left[\frac{\partial}{\partial x} (\mu \frac{\partial V}{\partial x}) + \frac{\partial}{\partial y} (\mu \frac{\partial V}{\partial y}) + \frac{\partial}{\partial z} (\mu \frac{\partial V}{\partial z}) \right] \quad (3.11b)$$

$$\rho \left(\frac{\partial W}{\partial t} + U \frac{\partial W}{\partial x} + V \frac{\partial W}{\partial y} + W \frac{\partial W}{\partial z} \right) + C = - \frac{\partial P}{\partial z} - \rho g + \left[\frac{\partial}{\partial x} (\mu \frac{\partial W}{\partial x}) + \frac{\partial}{\partial y} (\mu \frac{\partial W}{\partial y}) + \frac{\partial}{\partial z} (\mu \frac{\partial W}{\partial z}) \right] \quad (3.11c)$$

Where U V W are the velocity components in the x y z directions, P is pressure, ρ is the density of water, and μ is its effective viscosity.

Conservation of mass is considered as:

$$\partial P / \partial t + \rho c^2 (\partial U / \partial x + \partial V / \partial y + \partial W / \partial z) = 0 \quad (3.12)$$

Where, c is the speed of sound in water. Basically, water is incompressible but for mass conversion CFD considers it as compressible.

Engineers are interested in creating models that account for the diffusive character of turbulence rather than details of eddies. A popular turbulent model is the k - ϵ model. K is the intensity of the turbulence and ϵ is its local dissipation rate. Governing equations for this model are:

$$\begin{aligned} \partial k / \partial t + U \partial k / \partial x + V \partial k / \partial y + W \partial k / \partial z = T_P - T_D \\ + [\partial / \partial x (\mu/a \partial k / \partial x) + \partial / \partial y (\mu/a \partial k / \partial y) + \partial / \partial z (\mu/a \partial k / \partial z)] \end{aligned} \quad (3.13)$$

$$\begin{aligned} \partial \epsilon / \partial t + U \partial \epsilon / \partial x + V \partial \epsilon / \partial y + W \partial \epsilon / \partial z = D_P - D_D \\ + [\partial / \partial x (\mu/b \partial \epsilon / \partial x) + \partial / \partial y (\mu/b \partial \epsilon / \partial y) + \partial / \partial z (\mu/b \partial \epsilon / \partial z)] \end{aligned} \quad (3.14)$$

Where

$$T_P = G \mu_t / \rho \quad D_P = T_P C_1 \epsilon / k$$

$$T_D = C_D \epsilon \quad D_D = C_2 \epsilon^2 / k$$

$$\mu_t = C_3 k^2 / \epsilon \quad \mu = \mu_t + \mu_l$$

Where, $C_D=1.0$, $C_1=1.44$, $C_2=1.92$, $C_3=0.9$, $a=1.0$, and $b=1.3$ are constants based on data from geometrically simple experiments, μ_l is the laminar viscosity, μ_t is extra

viscosity due to eddy motion and G is a complex function of velocity gradient. In practice, the k - ϵ equations account for the convection, diffusion, production, and dissipation of turbulence. Equation 3.13 is an intensity equation where T_p is the production term and T_D is the dissipation term. Equation 3.14 is a dissipation equation where D_p is the production term and D_D is the dissipation term. The time averaging process introduces A , B , and C terms in the momentum equations. They are complex function of the velocity gradient. To simplify consideration of the sharp normal gradients in velocity and turbulence near a wall, special wall functions are used.

For the analysis in CFD, the flow field is discretized by a Cartesian system of grid lines. Small volumes or cells surround points where grid lines cross. If there is any fixed body in the flow, then flow is not allowed in the cells containing parts of fixed body. For general moving objects the position of the body keeps changing with time as the body is changing its position continuously. Boundary conditions are established, accordingly flow enter and leave the region of interest. Actually, CFD works on the governing equations of the flow. For CFD each governing equation is put into the form

$$\partial M / \partial t = N \quad (3.15)$$

For CFD, eq. 3.17 is the template which is applied to each governing equation at each point in a grid. The equations are integrated numerically across a time step. The time stepping equation is in the form of

$$M(t+\Delta t) = M(t) + \Delta t N(t) \quad (3.16)$$

Where the various derivatives in N are discretized using finite difference approximations. Algebraic equations for the scalars P , F , k , and ϵ at points where grid lines cross can be

found by the discretization and equations for the velocity components at staggered positions between the grid points.

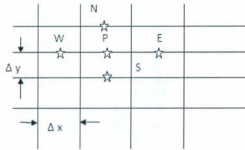


Figure 3.2 2-D Grid

Central differences are used to discretize the viscous terms in the momentum and turbulence equations. For a 2D grid, like Figure 3.2, if a diffusion term in the governing equations would be $\partial U^2 / \partial x^2$, this can be approximated by central differences like

$$\partial U^2 / \partial x^2 = \partial / \partial x (\partial U / \partial x) \approx [(U_E - U_P) / \Delta x - (U_P - U_W) / \Delta x] / \Delta x = (U_E + U_W - 2 U_P) / \Delta x^2$$

Again, most of the equations have convective terms, like $U(\partial U / \partial x)$. By using central differences it becomes

$$U(\partial U / \partial x) \approx U_P [(U_E + U_P) / 2 - (U_P + U_W) / 2] / \Delta x = U_P (U_E - U_W) / 2 \Delta x \quad (3.17)$$

This treatment of convective terms usually leads to numerical instability. To avoid this CFD codes use upwind difference. That gives

$$U(\partial U / \partial x) \approx U_P [(U_P - U_W) / \Delta x] \quad \text{flow from west} \quad (3.18a)$$

$$U(\partial U / \partial x) \approx U_P [(U_E - U_P) / \Delta x] \quad \text{flow from east} \quad (3.18b)$$

To ensure numerical stability, a combination of central and upwind differences is used for the convective terms. Sometimes upwind differencing generates a false diffusion. It makes the fluid appear more viscous. So, another scheme named skew differencing has been developed to counteract it. Collocation or lumping is used for the T and D terms. To march the unknowns forward in time, the momentum equations are used to update U, V, and W; the mass equation is used to update P and correct U, V, and W. The process is repeated until velocities and pressure both converge. The turbulence equations are used to update k, and ϵ [43].

3.7 Volume of Fluid

The volume of fluid concept is used to track water surfaces. A special function F is known as the volume of fluid or VOF function which is used to locate the surface of the water. Material volume considerations give:

$$\partial F / \partial t + U \partial F / \partial x + V \partial F / \partial y + W \partial F / \partial z = 0 \quad (3.19)$$

In CFD, for water F is taken to be unity and for air F is taken to be zero.

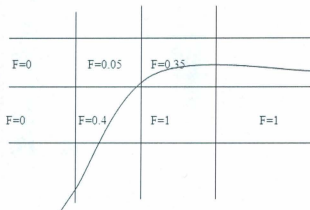


Figure 3.3 F Value in CFD Grid

Figure 3.3 shows a 2D view of the grid in CFD. However, F has got different value in Figure 3.3. If $F=1$, there is water in that grid, and if $F=0$, there is air in that grid. But F having a value in between 0 and 1 signifies the water surface. In the Figure 3.3, values of F determine the position of the water surface. The VOF equation, equation 3.22, is used to update F and the location of the water surface [43].

3.8 Moving Bodies in Flow

CFD can handle general moving objects. It can handle constant pressure bubbles in flow, such as, the air bubbles behind a body impacting a fluid surface. A moving body can be looked upon as a bubble with pressure that varies along its surface. The pressure must be such that it produces a bubble that has the same shape as the body. In fact, bubbles can be of any shape [46]. Figure 3.4 shows a triangular bubble where pressure acts from inside the bubble.

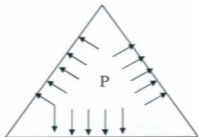


Figure 3.4 Pressure in a triangular bubble

Flow 3D can include moving objects. It allows more than one moving object in a problem. Each moving object can have different movement. The object moves with six degree of freedom or the movement of the object can be user defined. In this work, it has been worked with only one moving object that moves with six degree of freedom [43].

3.9 Conclusion

This chapter examines the theory for CFD. The next chapter discusses the experiments on the twisted Savonius turbine in Flow-3D. To find the fluid surface, the F value is calculated for every cell in the problem domain. Flow-3D has a feature volume of fluid for finding the F value.

Chapter 4

Experiments on the Twisted Savonius Turbine

4.1 Introduction

This chapter describes the experiments on the drag type device, the twisted Savonius turbine, which has been acknowledged to meet the design requirements for the North Atlantic Ocean Current. This chapter also discusses the equations that determine the characteristics of the turbine. The final section of this chapter deals with the turbine testing in the Flume tank. The turbine has also been tested in a wind tunnel, to observe its behavior in wind. Therefore, the results of the turbine in both water and wind have been studied.

4.2 Twisted Savonius Turbine

The twisted Savonius rotor is a vertical axis machine with a high starting torque and a reasonable peak power output [44]. The twisted Savonius rotor has an "S-shaped" cross-section. The concept of the Savonius rotor is based on the principle developed by Flettner [45]. The power from the rotor is based on the difference in pressure across the blade retreating from, and advancing into, the fluid. This is, in turn, related to the difference in the drag coefficients associated with the convex and the concave side of the blades [46, 47]. The Savonius rotor has a simple structure. Though it has good starting characteristics, it operates at relatively low speeds and has the ability to accept fluid from any direction. Its hydrodynamic efficiency is lower compared to other types of turbines,

like Darrieus and propeller rotors. The drag force of fluid acting on its blade is the driving force for the twisted Savonius. However, at low angles of attack, lift force also contributes to torque production [46]. Hence, the rotor is not a pure drag machine, but a compound machine, and can go beyond the limitation of C_p of a primarily drag type machine. Because of the high static torque, sometimes Savonius is used as the starter with other types of turbines having lower static torque, like the Darrieus Savonius Hybrid turbine. Though the static torque is high, it is not uniform at different rotor angles. At certain rotor angles, Savonius rotors cannot start on their own, as the coefficient of static torque is negative. The twisted Savonius design is very consistent in operation, and also has a much higher average power output compared to conventional ones. Therefore, the twisted Savonius is one of the best rotors for generating small scale power from a turbulent fluid flow. But the process of constructing a twisted Savonius turbine is extremely complex, requiring expensive materials and machinery, making the manufacturing cost very high. Though the conventional Savonius turbine has a very simple shape, the twisted version has a complex three dimensional geometry by comparison. The radius of the turbine is squeezed as the turbine is twisted, which occurs because of the geometric principles of the blade, not just the limitations of the materials. A greater angle of twist results in a greater potential efficiency in operation. Kamiji, Kedar and Prabhu completed experiments on a helical rotor [48]. The Savonius rotor and the twisted Savonius rotor both have the same cross sectional shape, like two semicircles in an 'S shape' throughout the turbine body, but three dimensional views are completely different. Figure 4.1 shows the CAD view of the conventional Savonius, and Figure 4.2

shows the three dimensional view of the twisted Savonius turbine. SolidWorks has been used to design the turbines.

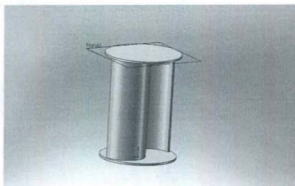


Figure 4.1 Conventional Savonius Turbine (Three Dimensional CAD View)

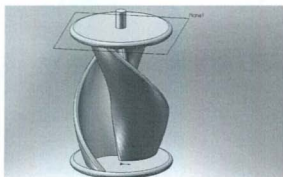


Figure 4.2 Twisted Savonius Turbine (Three Dimensional CAD View)

The twisted Savonius is somewhat similar to the Savonius, but it has a twist of 180° along its vertical axis. This is why it changes the direction of its body shape in every single step. Figure 4.3 shows the side view and the top view after removing the end plate of the turbine.

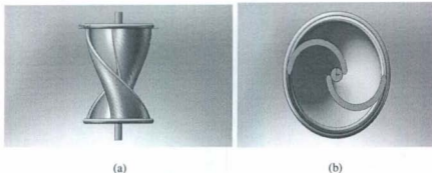


Figure 4.3 a) Left View (b) Top View (removing the end plate) of Twisted Savonius Turbine

A German physicist, Albert Betz, concluded in 1919 that no wind turbine can convert more than $16/27$ (59.3%) of the kinetic energy of the wind into mechanical energy, turning a rotor. To this day, this is known as the Betz Limit or Betz' Law. The theoretical maximum power efficiency of any design of wind turbine is 0.59. The concept of the Savonius rotor is based on the principle developed by Flettner. The coefficient of performance is of the order of 15% for Savonius [44]. Experiments on conventional Savonius rotors with an overlap ratio of 0.15 and an aspect ratio of 1.0 have been reported to have a maximum coefficient of power at 0.173 [49] and 0.17, when tested in

an open jet wind [50]. In an effort to improve the efficiency, minor changes are made in the shape of the conventional Savonius rotors, and these rotors have been referred to as modified Savonius rotors. A modified Savonius rotor with a shaft is reported to have a maximum coefficient of power of around 0.32 [51]. Figure 4.4 shows the efficiency of different types of turbines.

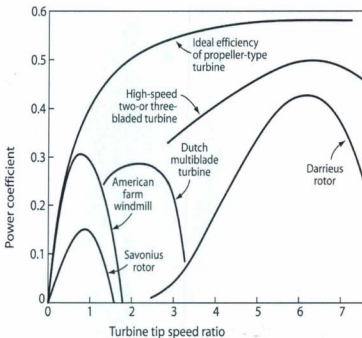


Figure 4.4 Power coefficient vs TSR Curve of Different Types of Turbines [48]

If a turbine is placed in the water, the power available in the area is

$$P_{\text{available}} = 0.5\rho A_s v^3 \quad (4.1)$$

Where $P_{\text{available}}$ is Power available in water (Watts)

ρ is Density of water (kg/m³)

A_s is (Height \times Diameter) = ($H_s \times D_s$), is the swept area of Savonius rotor (m²)

v = Velocity of water (m/s)

If C_p is the power coefficient of the twisted Savonius turbine, the power captured by the turbine is

$$P = P_{\text{available}} C_p \quad (4.2)$$

The tip peripheral velocity of the rotor is $U_s = \omega \times R$

Where, ω is the angular velocity of Savonius rotor

R (= $D/2$) is the radius of the Savonius rotor

Now the Tip Speed Ratio (TSR) of a Savonius turbine is defined as

$$TSR = \lambda = \frac{\omega R}{V} \quad (4.3)$$

The aspect ratio (A) represents the height (H_s) of the rotor relative to its diameter (D_s).

This is also an important criterion for the performance of the Savonius rotor:

$$A = \frac{H}{D} \quad (4.4)$$

There are a number of geometrical parameters that affect the efficiency of the Savonius rotor. Among these, the aspect ratio plays an important role in the hydrodynamic performance. Values of A around 4.0 seem to lead to the best power coefficient for a conventional Savonius rotor. As well, end plates lead to better hydrodynamic performances. The influence of the diameter D_r of these end plates in Figure 4.5 relative to the diameter D of the rotor has been experimentally studied. The higher value of the

power coefficient is obtained for a value of Df around 10% more than D , whatever the velocity coefficient [52]. There is another geometrical factor the called overlap ratio. It is expressed by

$$\beta = \frac{e}{d} \tag{4.5}$$

Where e is overlap between two buckets.

D is the diameter of each bucket shown in Figure 4.5.

Better efficiency can be achieved for β values of 0.2 to 0.3.

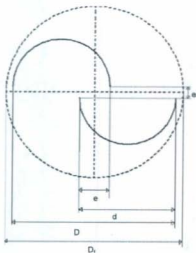


Figure 4.5 Top View of Twisted Savonius Rotor

4.3 Material Selection

In a marine environment, a sub-marine structure has to withstand salty water, abrasive suspended particles, and fouling growth. Therefore, it is challenging for a sub-marine structure to be there for a long time, because of the aggressive undersea environment. The designers first consider producing the required marine rotors in steel. However, achieving the necessary compound-curved profile in steel is expensive. Moreover, steel is very heavy, prone to fatigue, and susceptible to corrosion induced by salt water. Because of these disadvantages, a decision was made to use composites instead. If plastic materials are used, they ease the fatigue problem, both through their inherent fatigue tolerance and reduced blade weight. Temperature of the water is another issue, but the temperature range in water is much more limited than atmosphere making the material selection easier [53]. In this work, fiberglass has been used for building the twisted Savonius turbine prototype. Fiberglass is a fiber reinforced polymer made of a plastic matrix reinforced by fine fibers of glass. It is a lightweight and strong material. At the very beginning of the research work, it was planned to design a twisted rotor with ribs shown in Figure 4.6. But due to the complexity of this, the ribs were left out. The turbine itself has a complex geometry. It was impossible to build this turbine at the Technical Division of Memorial University. The Technical Division asked for a huge amount to get the turbine built from some other place, and this quote was too much to spend for the Seaformatics project.

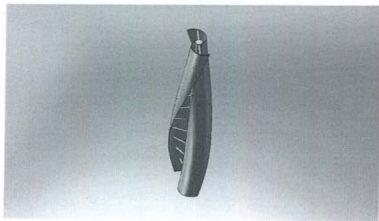


Figure 4.6 Twisted Savonius with Ribs

As a result, building a prototype of the turbine in the rapid prototype machine was attempted at Memorial University. Unfortunately, problems with the rapid prototype machine occurred. It could make 50% of the model perfectly, but after that machine could not remain in the proper track to build the model 100%, according to the design. At this time, Seacraft International was asked to build this turbine. They also asked a huge amount to build the full size turbine of 1 meter in height. At last, Mr. Wallace Robert, of Seacraft International, gave the prototype of the turbine free of charge to perform the experiments on it. The turbine used in this work is a handmade turbine, built by Wallace Robert, SeaCraft International.

4.4 Prototype of Twisted Savonius Turbine

Figure 4.7 shows the prototype of the twisted Savonius turbine. It is held vertically by using the frame that can be shown in Figure 4.7. The dimensions of the rotor are 18 inches in height and 6 inches in diameter. It has two endplates and does not have any central shaft. It does not have any gap between the two semicircular buckets.



Figure 4.7 Prototype of the Twisted Savonius Turbine

Characteristics for the prototype of the twisted Savonius turbine are as follows:

Height	18 inches or 0.4572 meter
Diameter	6 inches or 0.1524 meter
Overlap ratio	0
Aspect ratio	3
Swept Area	108 square inches or 0.07 square meters

4.5 Experimental Setup in Flume Tank

The twisted Savonius prototype was tested in the flume tank at the Marine Institute of Memorial University of Newfoundland, Canada. It contains 1.7 million liters of water in total. If the tank is full of water, it is divided into two sections: the upper and the lower section. The upper section is the test section and allows observation from above and from the side, and the lower section allows water to flow. In the return section, there are three impellers, or pumps, that are used to circulate the water around the tank. Each pump is driven by a 125 HP DC motor. The Flume tank in the Marine Institute is the world's largest tank of its type. The Flume Tank is 22.25 m long, 8 m wide and 4 m deep [54]. Water velocity began from 0.1 m/s. It increased by 0.05 m/s in every step, and the test results were recorded. 0.98 m/s is the highest current speed provided by the Flume tank. Figure 4.8 shows the turbine when it is submerged vertically in the water.



Figure 4.8 Testing of Twisted Savonius in Flume Tank

The turbine was hooked up with the frame and a shaft was taken out to integrate the load cell and the torque arm with it. The turbine was held with two bearings on the two ends with the frame. All the instruments were attached on the top of the turbine for data collection. The rotating shaft of the turbine is connected to a magnetic brake. The brake is imposed on the turbine by applying voltage across it. Voltage is proportional to the brake and once the brake is applied to it, it tries to stop the turbine. Voltage is increased until the turbine is fully stopped. During this time, data is encoded by the load cell. A 150mm long torque arm has been used in this experiment. The frame holding the turbine is attached with the platform above the Flume tank with a clamp. Angular speed is measured by the Nikon rotary encoder R X A 1000-22-1A attached on the top of the shaft. The encoder is shown in Figure 4.9.



Figure 4.9 Rotary Encoder

All the instruments, including load cell, torque arm, and rotary encoder, are connected with the DAQ system, where data are processed and fed to the laptop by USB. LabView has been used for the observing the data in the user interface. Figure 4.10 shows the complete set up for the twisted Savonius turbine in the Flume Tank.



Figure 4.10 Experimental Setup for Twisted Savonius

4.5.1 Test Results in Flume Tank

The turbine was tested in the Flume Tank at different current speeds. Currents varied from 0.1 m/s to 0.98 m/s. The turbine started to rotate when the current speed reached 0.4 m/s. The current speed in the tank was constant for different torque imposed on it by the attached magnetic brake. MATLAB has been used to plot the data. Figure 4.11 shows the rpm of the turbine considering data at different current speeds (Appendix A).

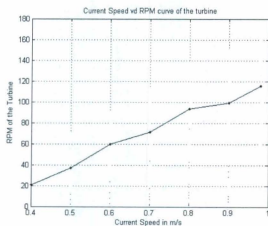


Figure 4.11 RPM at Different Current Speeds

Figure 4.12 shows the maximum power available at the turbine shaft at different current speeds. This curve has been generated, considering only the peak power at certain current speeds.

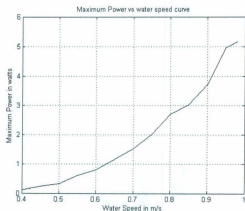


Figure 4.12 Maximum Power Output at Different Current Speeds

Figure 4.13 shows maximum power output of the turbine at different rpm of the turbine.

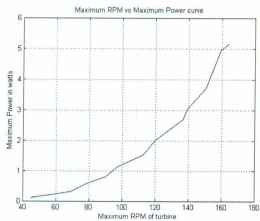


Figure 4.13 Maximum Power at Different RPM

In the experiment, data is recorded for different current speeds. If all the data are considered together, a curve can be generated using the bin method. Figure 4.14 shows the curve for the power output of the turbine vs current speed. This prototype can generate more than 2 watts at a current speed of 0.98 m/s, whereas theoretically it was expected to generate more than 3 watts at that speed. Friction causes this difference.

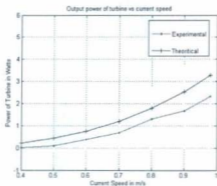


Figure 4.14 Turbine Output vs Current Speed Curve

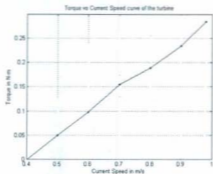


Figure 4.15 Turbine Torque vs Current Speed Curve

Figure 4.15 shows torque of the turbine at different current speeds. The C_p - λ curve for each individual current speed is shown in Figure 4.16. The bottom curve is at 0.4 m/s and gradually the current speed increases by 0.1m/s. After 0.4 m/s, the figure shows curves for 0.5 m/s, 0.6 m/s, 0.7 m/s, 0.8 m/s, 0.9 m/s, and 0.98 m/s.

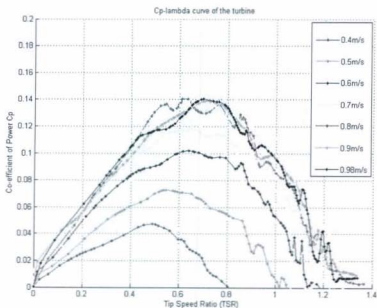


Figure 4.16 C_p - λ Curve at Different Current Speed

Figure 4.17 shows the C_p - λ curve for the twisted Savonius considering data at all the current speeds. The collected data has been smoothed with a span of 10%. A span of data has been considered and then smoothed by a moving average filter. The twisted Savonius turbine shows a peak efficiency of 12.50% around the Tip Speed Ratio of 0.8.

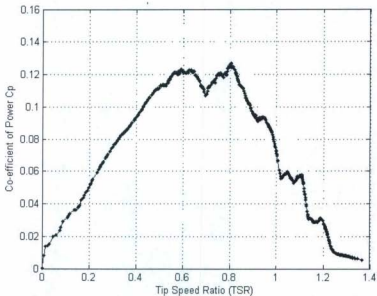


Figure 4.17 C_p - λ Curve of the Twisted Savonius

4.6 Wind Tunnel Test of the Twisted Savonius Turbine

The twisted Savonius turbine has also been tested in the wind tunnel. For wind tunnel testing, the turbine was mounted on a structure with a plate of higher diameter than the turbine. The plate of the structure was glued to one end of the turbine, and the plate was directly connected with the shaft. The turbine body was mounted vertically inside the wind tunnel. Other arrangements for instrumentation remain out of the tunnel, and the structure was attached to the wind tunnel's wooden floor using screws. Figure 4.18 shows the turbine inside the wind tunnel.



Figure 4.18 The Twisted Savonius in the Wind Tunnel

To measure data from the wind tunnel testing, the torque arm works as a brake too. Figure 4.19 shows the 100 mm long torque arm. When the turbine starts to rotate, the screw on the torque arm is tightened manually to apply the brake. The brake is applied to the turbine until it stops.

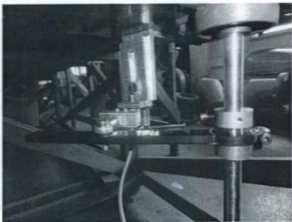


Figure 4.19 Torque Arm used in Wind Tunnel Testing

The torque arm does not cause any significant friction to the free rotation of the turbine. If the screw is tightened, the brake is applied to the turbine, and the load cell is already instrumented. At the bottom end of the shaft, a rotary encoder is attached to determine the angular speed of the turbine. One bearing is used, through which the turbine shaft passes toward the encoder. Figure 4.20 shows the instrumentation in the wind tunnel.

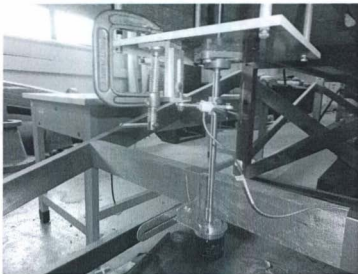


Figure 4.20 Instrumentation in the Wind Tunnel

4.6.1 Test Results at Wind Tunnel

The turbine has been tested for two wind speeds only. First the turbine has been tested at 10 m/s wind speed. Figure 4.21 shows the power coefficient vs TSR curve for the turbine in the wind tunnel. Figure 4.22 shows the power coefficient vs TSR curve for 13 m/s wind speed in the wind tunnel. For both 10 m/s and 13 m/s wind speed, the twisted Savonius shows 14% efficiency at a TSR of around 0.8.

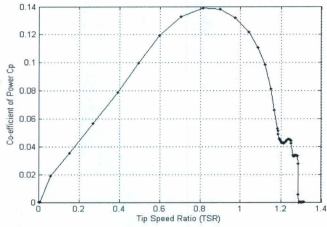


Figure 4.21 C_p - λ Curve of the Twisted Turbine at Wind Speed of 10 m/s

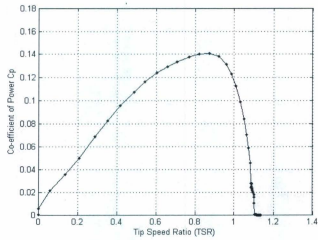


Figure 4.22 C_p - λ Curve of the twisted turbine at wind speed of 13 m/s

4.7 Conclusion

For the whole experimental set up, the proper combination of magnetic brake and load cell is very important. Vibration is a vital factor in the instrumentation of the system. The turbine was tested both in wind and water, and a magnetic brake was used to test the turbine in water. For wind tunnel testing, a torque arm with a screw was used for less friction and the brake was applied manually for different speeds. The same load cell and rotary encoder were used for testing in both wind and water. For both the experiments, it gives almost the same results. In water, it gives a highest efficiency of 13% around 0.8 TSR. In wind tunnel testing, the turbine has been tested for two wind speeds. At 10 m/s, the turbine shows 14% efficiency. At 13 m/s, it also gives 14% efficiency around 0.8 TSR. The turbine TSR remains within 1.4 for wind and water. The twisted Savonius turbine allows for better efficiency than the conventional Savonius turbine. Conventional Savonius gives 4.5% efficiency [55].

Chapter 5

Simulations of the Twisted Savonius Turbine in Flow-3D

5.1 Introduction

This chapter introduces the simulation of the turbine in a Computational Fluid Dynamics (CFD) environment. Flow-3D which is developed by Flow Science Inc. of Los Alamos, New Mexico, USA, has been used as a CFD software package. This chapter presents the CFD results of 180° and 90° twisted Savonius rotors, and focuses on the sensitivity testing of the mesh and drag model of the turbine. The sensitivity test of the mesh validates the mesh configuration for the simulations, and the Drag model gives a rough idea as to the efficiency of the turbine.

5.2 Computational Fluid Dynamics and Flow-3D

The solutions and proper visualizations of fluid dynamics problems are limited by their computational and design complexity. As these problems are associated with enormous numbers of differential equations, hand calculations are impossible. However, CFD has been introduced to solve fluid flow problems. CFD works with numerical methods, utilizing the Navier-Stokes and allied equations, to solve the fundamental nonlinear differential equations that describe fluid flow for predefined geometries and boundary conditions. CFD analysis results present a plethora of information, saving both money and time. Moreover, optimization of the analysis can easily be demonstrated. ANSYS FLUENT, ANSYS CFX, and Flow-3D are the most popular among the available CFD

software packages [56-58]. Flow-3D has been chosen for this work because of its exceptional features; most notably, Flow-3D can handle all sorts of complex phenomena, such as wave breaking, and phase changes including vaporization and solidification. No other CFD package can handle these phenomena. Flow-3D determines simulation results by investigating the dynamic behavior of fluids. It is particularly adept at solving time-dependent (transient), free-surface problems in one, two, and three dimensions. It also models confined flows and steady-state problems. Flow-3D can be applied to any kind of flow, because the program is written based on the fundamental laws of mass, momentum and energy conversion. Flow-3D is an all-inclusive package. No special additional modules for meshing or post-processing are needed. An integrated graphical user interface ties everything together, from problem setup to post-processing. FAVOR (Fractional Area /Volume Obstacle Representation) along with True VOF are also very powerful and unique features of Flow-3D. TrueVOF helps to track the location of free surfaces accurately, and to apply the dynamic boundary conditions to these surfaces. Flow-3D fluid modeling goes beyond the traditional Volume of Fluid technique to achieve the most accurate tracking of fluid surfaces to capture wave dynamics. In this research work, Flow-3D exhibits a magnificent visualization of real time turbine rotation, along with different data after the simulations. The simulations were run in Flow-3D version 9.4.1. An extensive discussion of the different tabs and options of Flow-3D, for running the twisted Savonius turbine simulations, has been presented in Appendix B [59].

5.3 Flow 3D Simulation Results

A series of different simulations were run in Flow 3D. Results are discussed in next sections.

5.3.1 Simulation Results of Twisted Savonius Rotor with Overlap Ratio

The twisted Savonius turbine has two end plates, but no central shaft. Rather, it has an overlap ratio of 35%. The turbine is 0.32 m high and has a diameter of 0.2286 m. Small shafts are attached to both end plates, in order to hook up the turbine. Figure 5.1 shows the CAD view of the turbine.

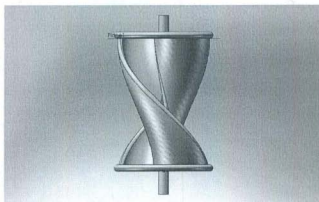


Figure 5.1 Twisted Savonius Rotor

The simulation was done for a set of variable torques at a constant current speed. The current speed was considered as 1 m/s for the simulations. The turbine was imported into

the mesh, and its cross sectional view is illustrated in Figure 5.2 by slicing the mesh along the z-axis. In Figure 5.2, the turbine has a gap between the two buckets.

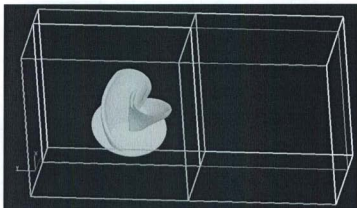


Figure 5.2 Cross Sectional View of the Mesh Block

A set of variable torques has been imposed on the body, and the angular speeds of the turbine are audited. The RPM of the turbine can be calculated from two dimensional analyses of the results.

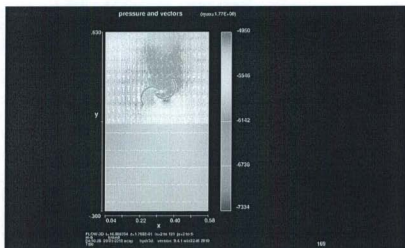


Figure 5.3 Time Frame at 16.8 Second



Figure 5.4 Time Frame at 17.1 Second

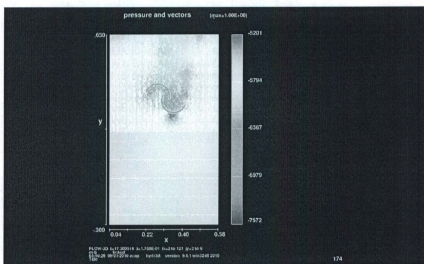


Figure 5.5 Time Frame at 17.3 Second

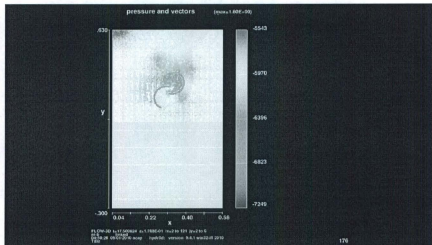


Figure 5.6 Time Frame at 17.5 Second

Figure 5.3-5.6 shows a complete revolution of the turbine. Flow-3D also generates the angular speed curve by itself, which is shown in Figure 5.7.

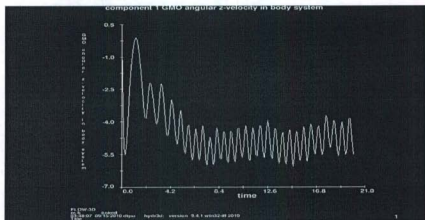


Figure 5.7 Angular Speed of the Turbine at $T=0.5$ Nm Torque

As angular speed is found from the simulation results and imposed torque is already known as an input parameter, the power available in the turbine shaft can be calculated.

$$P = \tau\omega \quad (5.1)$$

Where P is power captured by the turbine, τ is torque imposed on the turbine, and ω is the angular velocity of the turbine. The power coefficient can be calculated from Equation 4.2. The Tip Speed Ratio (TSR) can be calculated from Equation 4.3. MATLAB has been used to plot the C_p - λ curve of the twisted Savonius rotor. Figure 5.8 shows the C_p - λ curve of the twisted Savonius having an overlap ratio of 35%.

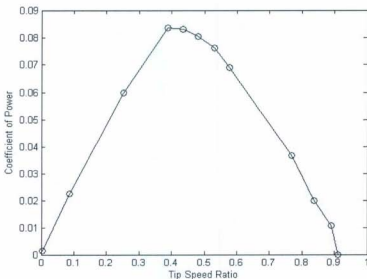


Figure 5.8 C_p - λ Curve of Twisted Savonius Turbine

The twisted Savonius turbine with 35% overlap ratio shows more than 8% efficiency, at a TSR of 0.388.

5.3.2 Simulation Results of Twisted Savonius Rotor with a Zero Overlap Ratio

Simulations have been run in Flow-3D for the twisted Savonius with a zero overlap ratio. This turbine does not have any gap between the two buckets. A CAD view of the turbine is given in Figure 5.9.

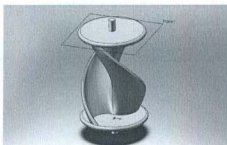


Figure 5.9 Twisted Turbine with Zero Overlap Ratio

A cross-sectional view of the turbine is given in Figure 5.10, slicing the mesh when the turbine is imported in it.

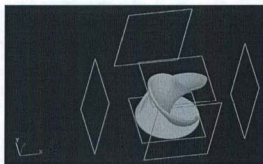


Figure 5.10 Mesh Slice with Zero Overlap Ratio

This simulation was done under same environment as the previous one. The turbine's angular speed was observed for a set of variable torques. Figure 5.11 displays the simulation results.

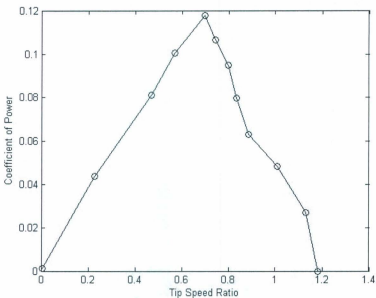


Figure 5.11 C_p - λ Curve of Twisted Savonius Turbine with Zero Overlap Ratio

This twisted Savonius turbine with no overlap provides better efficiency compared to the twisted Savonius turbine with the overlap ratio. It shows a maximum efficiency of 12%, whereas the turbine with the overlap ratio gives 8% maximum efficiency. Turbine with zero overlap provides maximum efficiency around 0.7 TSR. The maximum TSR for this type of turbine is close to 1.2, whereas it is 0.9 in case of the turbine with the overlap ratio. Experimental testing has been performed for a turbine with a zero overlap ratio and

the experimental results validate the simulation results. The turbine shows a maximum 12% efficiency around 0.7 TSR both in experiment and simulations. Though the prototype of the turbine has different dimensions than the simulated one, the C_p - λ curve is almost same for both cases. This is because of the scaling laws.

5.3.3 Horizontally Mounted Position-1 for the Twisted Savonius Turbine

The twisted Savonius turbine has been regarded as a vertical axis water current turbine in the previous simulations. This topic, however, highlights the twisted Savonius as a horizontal axis turbine. In this simulation, the x-axis is indicated as the axis of rotation of the rotor. The rotor, as studied in this simulation, has an overlap ratio. Figure 5.12 shows the turbine when it is imported in the mesh.

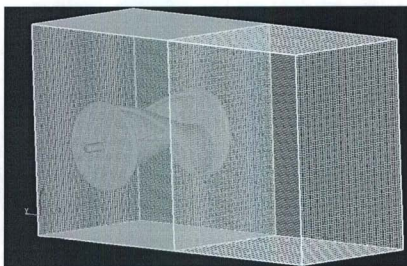


Figure 5.12 Twisted Savonius as a Horizontal Axis Turbine

Current swipes the turbine from the negative y-axis. Simulations have been carried out to allow a comparative study among turbine angular speeds, for different positions. There is a small variation of RPM between this position and the previous position. For 1m/s current, the turbine rotates at 85 rpm, whereas for rotation around the z-axis, the twisted Savonius with an overlap ratio rotates at 83 rpm for freewheeling. Accordingly, the following two axes of turbine rotation endorse the same $C_p-\lambda$ curve.

5.3.4 Horizontally Mounted Position-2 for Twisted Savonius Turbine

In this simulation, some changes have been made to the structure of the turbine. Two end plates have been removed, and a central shaft has been attached in between the two buckets. Figure 5.13 shows the CAD view of this turbine.

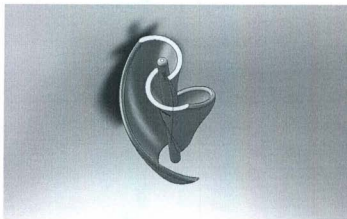


Figure 5.13 Twisted Savonius Turbine with No End Plates

The turbine has been mounted according to Figure 5.14 in Flow-3D, in order to study its angular speed.

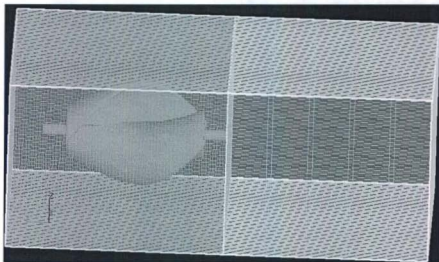


Figure 5.14 Horizontally Mounted Turbine at Position 2

In this case, the axis of rotation is the y-axis. Currents move towards the rotor from the negative y-axis. Under this condition, Figure 5.15 shows the C_p - λ curve of the turbine. The turbine gives 14% efficiency for this position, at approximately 0.7 TSR.

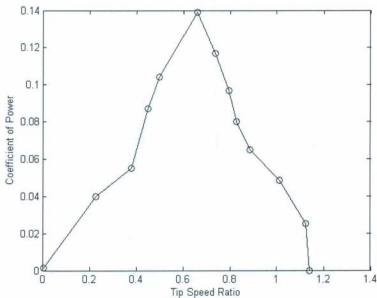


Figure 5.15 C_p - λ Curve for Horizontally Positioned

5.3.5 Simulation of a Quarter Pitched Savonius Turbine

This thesis also considered a quarter pitch twisted Savonius rotor, and estimated its performance using Flow-3D. The rotor has 0.35 overlap ratio. It has two endplates with two small shafts attached. Figure 5.16 shows the CAD drawing of this turbine.

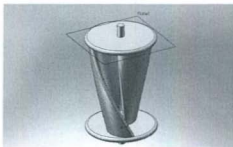


Figure 5.16 Quarter Pitch Twisted Savonius Turbine

In the simulations, the current speed was set up at 1 m/s. The rotational speed of the rotor goes through a transition state to reach the steady state within a few seconds. The simulation results show that the quarter pitch twisted Savonius attains an efficiency of 7%, at a TSR of approximately 3.6. Figure 5.17 shows the C_p - λ curve of the quarter pitch twisted Savonius turbine.

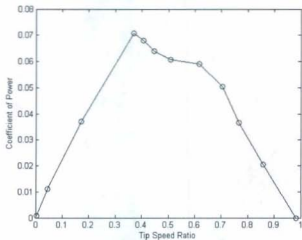


Figure 5.17 C_p - λ Curve of Quarter Pitch Twisted Savonius Turbine

5.4 Sensitivity of Mesh

To examine the sensitivity of the results to the size of the mesh, three different meshes were used for the mesh block 1 which holds the turbine. The standard mesh used 144 cells in the x and y directions and 44 cells in the z direction. For freewheeling of the turbine, it gives 84 RPM. When a mesh with 160 cells in x and y direction and 50 cells in z direction was used, the simulation gave 85 RPM. Figure 5.18 shows the angular speed. When a mesh with 136 cells in x and y direction and 44 cells in z direction was used, it gave 84 RPM. So the standard mesh seems adequate. Simulation results also agree with the experimental results.

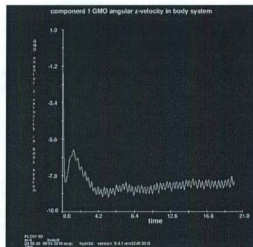


Figure 5.18 Angular Speed of the rotor

5.5 Drag Model

Figure 5.19 shows the cross sectional view of the basic Savonius turbine.

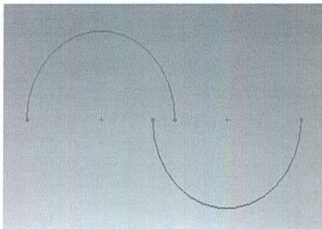


Figure 5.19 Schematic of Basic Savonius

If a current is flowing downwards in Figure 5.19, a wake drag load would be produced at the bottom of the right bucket and a stagnation pressure load would be produced at the top of the left bucket. The gap between the buckets would tend to make pressure roughly the same at the center of each bucket. This pressure would be roughly the stagnation pressure. Each of the bucket loads has a moment arm. It creates a torque about the rotor axis. Multiplying torque by angular speed gives power. The twisted Savonius turbine can be considered to be made of up of a large number of basic Savonius strips as shown in Figure 5.20. Summing the power of the strips gives an estimate of the total power from the turbine.

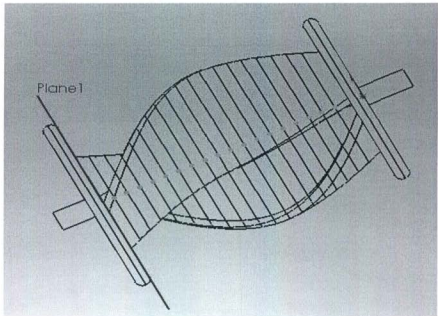


Figure 5.20 Strip Model of Twisted Savonius

Figure 5.21 gives a power coefficient versus tip speed ratio based on the strip model. It assumed a drag coefficient of 2 for the left bucket and a drag coefficient of 0 for the right bucket. It gives a power coefficient peak of around 0.09 at a tip speed ratio around 0.8. This is obviously very rough but it does give roughly the same result as the CFD simulation and the tests.

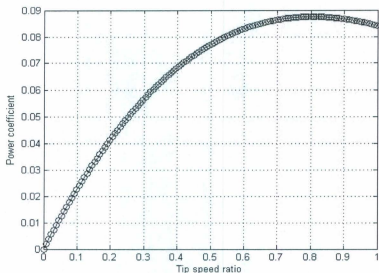


Figure 5.21 Strip Model Power

5.6 Conclusion

Flow-3D offers a significant number of features to work with. The main objective is to deploy this turbine under the ocean on the seabed, so the simulations have been performed in the underwater environment. The simulation results determine that the twisted Savonius turbine can achieve more than 8% efficiency, which is higher than the conventional Savonius [34]. If there is no gap between the two buckets, the efficiency increases. The efficiency of the turbine has been studied for different positions of mounting. If the turbine has an x-axis or z-axis as axis of rotation, they give almost the

same angular speed. If the turbine has the y axis as the axis of rotation then the turbine speed ramps up compared to the other two positions, giving more than 90 rpm. Different types of results have been studied with Flow 3D, without any expensive experimental setup.

Chapter 6

Marine Current Energy Conversion System

6.1 Introduction

The concept presented here is based on a twisted Savonius rotor coupled with a Permanent Magnet Generator (PMG), to convert the marine current energy into electrical energy for self-powering the Seaformatics pods. This coupling can be either direct drive or geared. Presently, direct drive coupling is becoming popular because of its simplicity. This chapter discusses the PMG and the design and implementation of a boost converter, along with the Maximum Power Point Tracking (MPPT) algorithm. In the proposed MPPT algorithm, the Tip Speed Ratio (TSR) of the turbine and generator's coupling shaft has been optimized based on the perturbation and observation method. A marine current turbine emulator has been developed to test the electrical system in the lab. However, this chapter focuses on the elements to convert the mechanical energy into electrical energy.

6.2 The Twisted Savonius Water Current Turbine Emulator

The twisted Savonius turbine is used to convert water current into mechanical energy, which is converted to electrical energy by a PMG. A twisted Savonius rotor emulator was implemented to test the power electronics elements in the lab. The emulator develops the torque on the PMG's shaft. A manual control of variable supply has been utilized to vary motor shaft speed, as the torque, developed on the motor shaft, is proportional to the armature current. The motor basically mimics the shaft angular speed generated by a full

size twisted Savonius turbine of 0.33 m^2 swept area, with an aspect ratio of 3 and a 1:4 gear ratio. This set up performs only the steady-state analysis of the system. Figure 6.1 shows the water current turbine emulator.

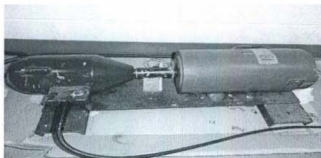
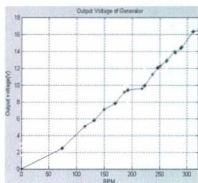
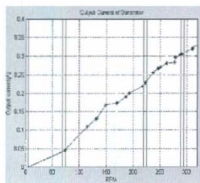


Figure 6.1 MCEC Emulator

Figure 6.2 illustrates generator output voltage and current with respect to angular speed [60].



(a)



(b)

Figure 6.2 Output (a) Voltage and (b) Current of Generator at Different RPM

6.3 Generator

Although many people focus on the gear box to couple the turbine, direct drive requires fewer components, less maintenance and lower cost [61-63]. A recent study suggests that a generator coupled with a gear box is more prone to failure [64]. Because of these concerns, direct drive is gaining popularity.

The electrical frequency of the generated voltage can be determined by the number of poles in the generator, and the angular speed of the rotor expressed in RPM.

$$f = \frac{P}{2} \frac{n}{60} \quad (6.1)$$

According to equation 6.1, electrical frequency is directly proportional to the number of poles. If the number of poles is high enough to achieve the frequency, it makes the size of the machine bigger, as RPM is lower in direct drives. In the case of a vertical axis water current turbine, the size of the generator has less impact [65]. But, for a wide range of water speed operations, direct coupling is more popular because of fewer rotating parts.

The generator works on the principle of Faraday's Law of induction. The time-varying electromotive force (emf) or induced voltage in a close circuit is equal to the change of magnetic flux through the circuit.

$$E(t) = -N \frac{d\Phi}{dt} \quad (6.2)$$

Where $E(t)$ is the induced emf, N is number of turns of coil in stator, and Φ is flux through the closed path.

The electromotive force induced in the coil depends on some of the parameters. These are the number of turns in the winding N , electrical frequency f , and amplitude of magnetic flux density B_m . Equation 6.3 shows the relation among them:

$$E(t) \propto NfB_m \quad (6.3)$$

6.3.1 Generator Losses

A generator cannot convert the full input mechanical energy into electrical energy because it has some sources of loss. A generator has both mechanical and electrical losses, which is contributed to by friction in the bearing and commutator, and air friction in rotating armature. There might also be vibration in the system, which is a kind of mechanical loss.

There are two types of electromagnetic losses: copper losses and iron losses. Copper losses are basically resistive losses in the windings. Copper losses can be calculated by equation 6.4.

$$P_{Cu} = R_g I_a^2 \quad (6.4)$$

Where R_g is the internal resistance of the generator and I_a is the armature current.

There are three kinds of iron losses in the generator: hysteresis losses, eddy current losses and excess losses. Because of the reversal of the magnetization of the laminated iron stator core, Hysteresis losses occur [66].

$$P_{Hysteresis} \propto B_{max}^2 fV \quad (6.5)$$

Where, B_{max} is maximum flux density, f is electrical frequency, and V is volume of the stator. Actually, hysteresis losses are an inherent property of the generator's material. The loss cannot be entirely avoided, but can be reduced.

During the operation of a generator, a current is induced in the winding. Sometimes a current is also induced in the stator iron [67]. This is called eddy current loss. It depends on maximum flux density B_{max} , frequency f , thickness of lamination d , and volume of stator V .

$$P_{eddy} \propto B_{max}^2 f^2 d^2 V \quad (6.6)$$

In some of the literature, excess losses are mentioned [68], such as

$$P_{excess} \propto (B_{max} f)^{3/2} V \quad (6.7)$$

6.4 Permanent Magnet Generator

To convert mechanical energy into electrical energy in renewable energy applications, different kinds of generators can be coupled with the turbine, such as:

- Squirrel-Cage rotor Induction Generator (SCIG)
- Doubly-Fed Induction Generator (DFIG)
- Wound-Rotor Induction Generator (WRIG)
- Permanent Magnet Generator (PMG)

A PMG can be used for a wide range of applications. It can be utilized in low speed applications, like gearless wind and hydro applications, as well as in high speed applications in some regenerative and co generative technologies [69]. A PMG can be of

different types, such as with surface mounted magnets, buried magnets, and damper windings. Moreover, PMGs possess several advantages over electrically excited machines:

- Higher efficiency
- Permanent magnets are used, so it does not require further power supply for magnetic field excitation
- Better reliability because of absence of mechanical components like slip rings
- Improved thermal characteristics due to absence of field losses
- Higher power to weight ratio

However, a PMG has some drawbacks including cost and demagnetization at high temperature. As time passes the performance is increasing, and the cost is decreasing. For these different features, PMG technology is becoming more attractive for direct drive applications [70]. Figure 6.3 shows a cross section of a typical PMG.

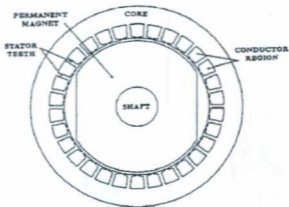


Figure 6.3 Cross Section of a PMG

6.4.1 Cogging Torque

Cogging torque is an inherent property of a permanent magnet generator, due to its geometry. It can be reduced in different ways. It has an influence on the generator's self starting capability, and it produces noise and vibration when the generator runs. Cogging torque is produced in the generator shaft when it rotates, with respect to stator, at the no load condition.

6.4.1.1 Starting of a Turbine

To get the best output from a turbine, it should be operated at the maximum power coefficient point. According to equation 4.3, TSR is a function of the angular speed of the turbine. At the beginning of rotation, angular speed is very low; hence, TSR is also low, giving a low value for C_p . Ultimately, hydrodynamic efficiency of the turbine falls. If the

turbine is direct coupled with the generator, then cogging torque has a negative impact on starting the generator. Thus, cogging torque should be low at the beginning; otherwise, it is hard to start rotating with the small C_p overcoming the cogging torque. Sometimes, the turbine may remain in a locked condition if the cogging torque is too high.

6.4.1.2 Turbine Running Condition

The small turbine has lower inertia compared to the large one, as it has smaller blades and less mass. The turbine structure is excited by the cogging torque, and the inertia smoothing effect is not significant. This is more obvious in cases of smaller turbines. During low current speed, a lower angular speed develops; as a result, cogging torque, noise, and vibration increase in the system. This kind of vibration causes problems for the integrity of the mechanical structure. At a high current speed, the turbine rotates at a higher angular speed. During this period of high speed, the kinetic energy stored in the turbine and torque in the shaft is significantly higher than the cogging torque.

6.4.2 Reduction of Cogging Torque

Cogging torque can be reduced in several ways:

Magnetic pole shape: Sometimes, magnetic poles in the generator have such a shape that there are uniform air gaps in the rotor. If the shape of the poles resembles a loaf of bread, the air gaps in the rotor are non-uniform, which causes reduction in the cogging torque.

Pole width to optimum pole width ratio: If pole width is changed, the cogging torque varies. If the optimum pole width is reached, cogging torque comes to a reduced value. In cases other than optimum pole width, cogging torque increases.

Skewing Effect: Skewing the stator stack or magnet pole can almost eliminate the cogging torque in a PMG. But, this raises the system complexity and cost.

6.5 Twisted Savonius Testing with Generator

The turbine has been tested in the wind tunnel, having been coupled directly with a dc motor to study the electrical output of the twisted Savonius turbine. The objective was to get electrical energy from freewheeling of the turbine regardless of the rating of the generator. Figure 6.4 shows the experimental setup in the wind tunnel.



Figure 6.4 Turbine Coupled with Generator in the Wind Tunnel

Generator output was connected with a 50 ohm resistor. Data has been collected for different wind speeds. Figure 6.5 shows voltage at different wind speeds.

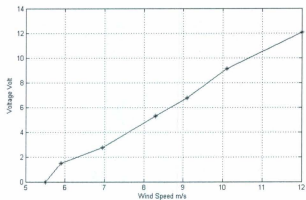


Figure 6.5 Wind Speed vs Voltage Output Curve

Figure 6.6 shows current output at different wind speeds.

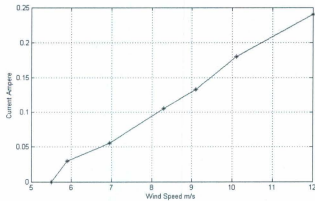


Figure 6.6 Wind Speed vs Current Output Curve

Figure 6.7 shows power output of the generator at the following wind speeds.

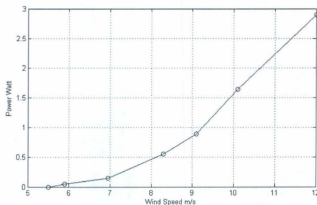


Figure 6.7 Wind Speed vs Power Output Curve

6.6 DC – DC Converters

A dc-dc converter converts dc voltage from one level to another level. A dc-dc converter is like a dc equivalent to an AC transformer with a continuous variable turns ratio. A dc-dc switch mode converter converts the unregulated dc into controlled dc output. The net power input must be equal to the output power, so, no energy generation occurs in the converter; rather, there are losses because of its components. The power flow in a converter is

$$P_{in} = P_{out} + P_{losses} \quad (6.8)$$

Where P_{in} is the input power to the converter

P_{out} is the output power from the converter

P_{losses} is the power losses in the converter

For ideal converters, $P_{\text{losses}} = 0$ in equation 6.8. In fact, there are no ideal converters in real world. All converters have losses. For an ideal converter

$$P_{\text{in}} = P_{\text{out}}$$

$$\text{Or, } V_{\text{in}} \times I_{\text{in}} = V_{\text{out}} \times I_{\text{out}}$$

$$\text{Or, } V_{\text{in}}/V_{\text{out}} = I_{\text{out}}/I_{\text{in}} \quad (6.9)$$

If voltage is stepped up then current has to be stepped down in the output according to equation 6.9.

Efficiency of a converter is

$$\text{Efficiency} = (P_{\text{out}}/P_{\text{in}}) \times 100\% = P_{\text{out}} / (P_{\text{out}} + P_{\text{losses}}) \times 100\% \quad (6.10)$$

The dc-dc converters can be used for motor control in automobiles, marine hoists, and mine haulers. They can also be used for the regenerative braking of a dc motor, in dc voltage regulators, and in conjunction with an inductor to generate a dc current source.

There are different types of dc-dc converters. Depending upon the dielectric isolation, converters can be classified into two different types:

- Non Isolating converters
- Isolating converters

If voltage is stepped down or up in a small ratio, then non isolating converter are used.

Non isolating converters can be of different types:

- Buck converters
- Boost converters

- Buck- Boost converters
- Cuk converters
- Full-bridge converter

Isolating converter can be divided into two types:

- Flyback type
- Forward type

Buck converters can step down the voltage level, whereas a boost converter steps up voltage level. Buck-Boost is the combination of buck and boost type converters. It can either step up the voltage or step down. But, the output of this type of converter is of an opposite polarity relative to the input. A Cuk converter does the same thing as buck-boost converters, in that it also inverts the polarity of the output voltage. But, a Cuk converter has less current ripple. The gain of the converter depends on the duty ratio. Figure 6.8 shows the gain vs duty ratio curve for different converters.

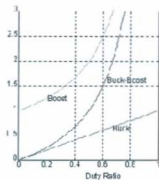


Figure 6.8 Gain vs Duty Ratio Curve for Different Converters

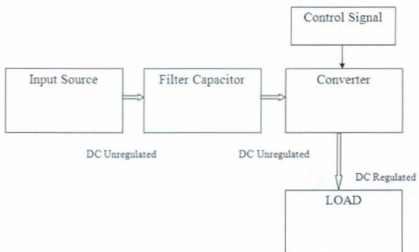


Figure 6.9 DC-DC Switching Mode Converter System

Figure 6.9 shows the dc-dc converter system. The input source may be either the rectifier output, or the battery output to the converter. The input filter capacitor lessens the ripple, and then the supply goes to the converter. A control signal is also sent to the converter, to alter the voltage to the desired level. In the output, a small filter can be used that is an integral part of the converter. The output of the following system feeds a regulated dc to the load.

6.6.1 Boost Converter

A boost converter has been clinched to implement in the proposed system. Figure 6.10 shows the circuit diagram of the boost converter. The supply voltage is V_s , and it is assumed constant throughout its operation. M is the MOSFET, L is inductance, D is the diode, and C is capacitance in the circuit diagram.

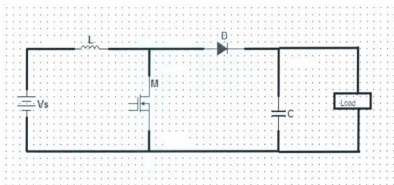


Figure 6.10 Boost Converter

A Boost converter has two modes of operation: Continuous mode and Discontinuous mode. The waveforms for the continuous mode of operation are shown in Figure 6.11. All the waveforms have been presented in the same time scale in Figure 6.11. V_s is the supply voltage, I_s is the source current and I_L is the inductor current, V_c is the capacitor voltage and V_o is the output voltage.

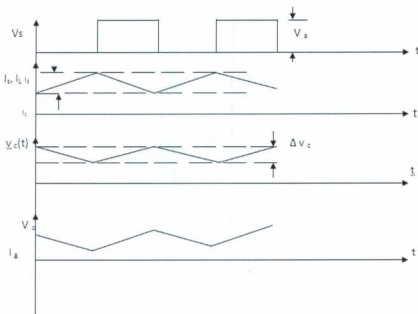


Figure 6.11 Waveforms for Boost Converter

Discontinuous Mode

If the inductor current falls to zero before the next cycle comes, the operation of the boost converter is called Discontinuous Mode. Figure 6.12 shows waveforms of the boost converter for discontinuous mode of operation.

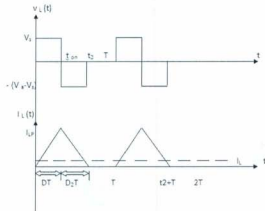


Figure 6.12 Voltage Current Waveforms for Discontinuous Mode Operation

An extensive discussion of continuous and discontinuous mode of operations is presented in Appendix C [71-73].

6.6.2 Design of a Boost Converter

Figure 6.13 shows the schematic of the proposed Boost converter in this research work. The parameter values have been chosen based on the different equations of boost converter (Appendix D). A microcontroller based control system restrains the switching of the logic level MOSFET, which has $V_{GS} = 5$ volt. Microcontroller supplies controlled signals with 20mA current to turn ON and OFF the MOSFET. Table 6-1 shows the required components to implement the converter. Different converters with comparatively higher rating are available in the market. None of them are compatible with this work. If a customized one is ordered, that would take higher cost. So, the converter has been constructed for this work.

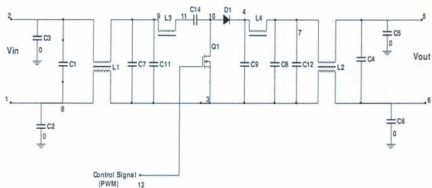


Figure 6.13 Schematic of Boost Converter

Table 6-1 Components for building the boost converter

Component	Value/Description	Quantity
C1,C2,C3,C4,C5,C6	Electrolytic Capacitor 0.01 μ F	6
C7,C12	Electrolytic Capacitor 250 μ F	2
C8	Electrolytic Capacitor 470 μ F	1
C9,C11	Electrolytic Capacitor 680 μ F	2
L1	Inductor 150 μ H	1
L2	Inductor 260 μ H	1
L3,L4	Inductor 380 μ H	2
Q1	MOSFET IRF630	1
D1	Diode MUR815	1

Figure 6.14 shows the Boost converter built in the lab.



Figure 6.14 Proposed Boost Converter

Figure 6.15 shows the input voltage vs output voltage curve for the designed converter.

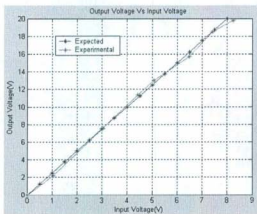


Figure 6.15 Input vs Output Voltage of the Boost Converter

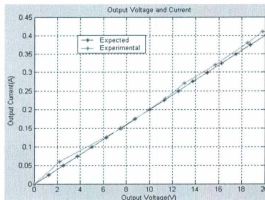


Figure 6.16 Input vs Output Current of the Boost Converter

Figure 6.16 shows the input current vs output current curve for the designed converter (Appendix D). Figure 6.17 shows the input voltage vs output power curve for the designed converter [60].

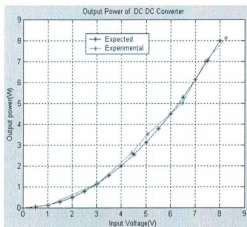


Figure 6.17 Input Voltage vs Output Power of the Converter

A converter has various sources of loss, such as inductor resistance and MOSFET switching. The diode has a forward biased voltage drop. There are also losses in the capacitors used in the converter. Because of these losses, converter efficiency is reduced. The designed converter has an efficiency of 65%. For dc-dc converters, switching loss is a major source of loss.

6.7 Maximum Power Point Tracking Algorithm (MPPT)

In the MCECS, MPPT is implemented to achieve an optimized power output at variable turbine speeds. MPPT works on the dc-dc converter to match the turbine output with the battery charging. Basically MPPT concept originated from algorithm used in PV cells system. MPPT seeks to deliver maximum power to the load. There are several algorithms used to implement MPPT. These are:

- Perturbation and Observation Method
- Incremental Conductance Method
- Constant Voltage method

Some research uses the sign of the difference power ΔP . Depending on the sign of ΔP , the duty ratio of the PWM signal varies. PWM variation rate is established by CPU register of the microcontroller [74]. Sometimes, a dummy load is used if the supply voltage is greater than the rated value [75]. Several studies have implemented MPPT with a capacitor in series with the battery thus achieving higher efficiency [76].

6.8 Proposed MPPT Algorithm

The Perturbation and Observation method is the most commonly used MPPT algorithm. In most cases, voltage, current, or power is perturbed in an iterative cycle. When a steady state is reached, the system operating point oscillates around the MPP. The oscillation amplitude depends on the step size of perturbation, causing some power loss. For very fast varying systems, this algorithm fails to track the MPP. In this work, the Perturbation and Observation method has been applied to optimize the TSR of the turbine. The C_p - λ curve of the flume tank testing has been discussed in Chapter 4. The MPPT controller has been aimed to operate the turbine at 0.7 TSR, so it will exhibit the maximum efficiency. The instantaneous TSR is perturbed in every cycle to reach the steady state. Once the steady state is reached, it keeps oscillating around that optimum TSR.

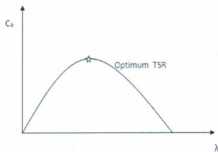


Figure 6.18 Perturbation and Observation Method Control Action

At the optimum TSR, turbine efficiency is highest (Figure 6.18). So, at the maximum point

$$dC_p / d\lambda = 0$$

If an instantaneous TSR is larger than the optimum one, then there is positive action to return back to the optimum TSR. Accordingly, if an instantaneous TSR is lesser than the optimum TSR, then negative action to go forward to the optimum TSR.

Figure 6.19 shows the flow chart of the algorithm. Input current and voltage, along with output current and voltage, are collected by the ADC. A speed sensor encodes the angular speed of the shaft. Data are logged in the computer and displayed in the HyperTerminal of the computer, as well as in a LCD display attached with the control unit. Angular speed of the generator shaft is taken iteratively, and it is compared with the optimum speed of the shaft at which the turbine gives its maximum efficiency. If the shaft speed is higher than the optimum one, then the width of the PWM is increased to manage the load, in order to slow down the angular speed at the optimum speed. Again, if the shaft speed is lower than the optimum speed, width of the PWM is decreased to speed it up to the optimum speed. If the shaft remains at the optimum speed, then the same width of PWM is supplied to the switch. PWM remains within a predefined maximum and minimum range.

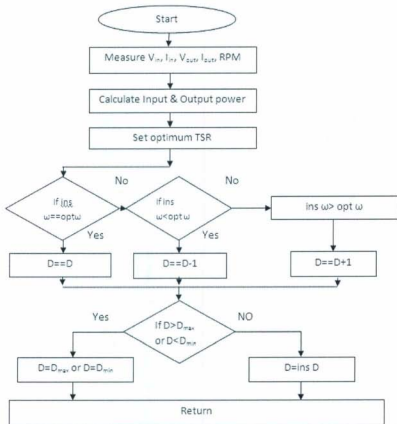


Figure 6.19 Flow Chart of MPPT Algorithm

The code has been written in programming language C. CCS C compiler has been used that is not ANSI C compatible. The programming code has been given in Appendix D. Serial port was used to log the data and to debug.

6.8.1 Hardware Setup

The system operates around the optimum TSR because of the MPPT algorithm. Output of the converter is fed to the battery until it is charged to its rated value. Figure 6.20 shows the laboratory setup of the energy conversion system.

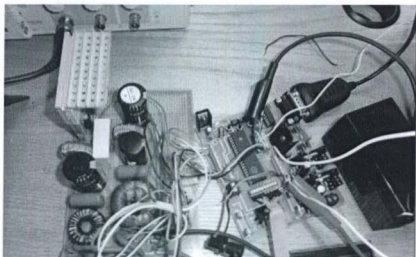


Figure 6.20 Hardware Setup

To implement the control strategy, low power consumption CMOS microcontroller PIC16f877 has been used. It is a 16 bit, four channel microcontroller, having 39.2 kHz maximum frequency when it is driven by 20 MHz clock. It has two PWM outputs those are fully controllable. One of them has been used to supply control signal to the MOSFET of the boost converter. Port D has been used for display data on the LCD screen. A Toshiba Satellite Pro with Intel (R) Core (TM) 2 Duo CPU of 2 GHz has been used to program, and load the program to the microcontroller. Observing the instantaneous

angular speed of the rotor shaft is the most important factor in this case. In order to measure the angular speed of the rotor shaft, a high resolution encoder with 256 cycles/rev has been used. The encoder is from Grayhill. The sensors and signal conditioner of the system are connected to the microcontroller A/D converters.

6.8.2 Results

The MPPT algorithm has been developed to extract maximum power from the turbine. The turbine is run in the optimum TSR based on PWM signal supplied to the converter. For experimental purposes, a generator shaft was run at an optimum speed of 8 rad/sec. Figure 6.21 shows the stabilization of speed at 8 rad/sec. Figure 6.22 shows the PWM generated through this mode of operation. PWM with a higher width is supplied to the switch, to reduce the angular speed to the optimum speed.

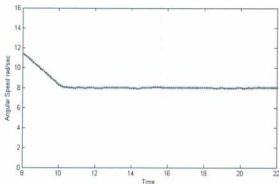


Figure 6.21 Angular Speed falls to 8 rad/sec

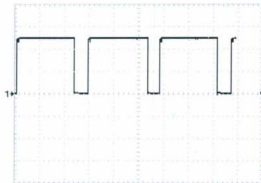


Figure 6.22 PWM to reduce Angular Speed

Once the optimum angular speed is achieved, the width of the PWM keeps oscillating around the steady state level. During t_{on} PWM has an amplitude of 5 volts. In Figure 6.19, each square along y axis is 2 volts. Figure 6.23 shows the PWM signal width oscillation around 930 with time when angular speed is at the optimum speed. Y axis is the value of PWM width defined in the program code (Appendix E).

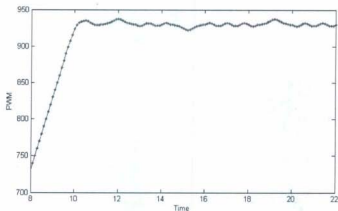


Figure 6.23 PWM Signal Variation at Optimum Speed

If the generator runs at a lower speed compared to the optimum speed, then it is speed up by reducing the load. A smaller PWM is supplied to the converter. Figure 6.24 shows a stabilization of speed at 8 rad/sec for lower speed.

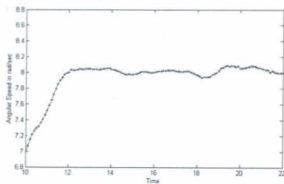


Figure 6.24 Angular Speed Stabilizes around the Optimum Speed

Figure 6.25 shows the PWM signal generated in this mode of operation.

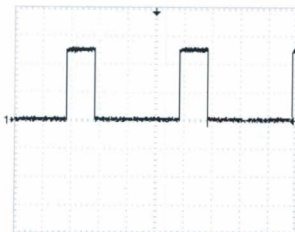


Figure 6.25 PWM to increase Angular Speed

6.9 Voltage Sensor

A voltage sensor is nothing but a voltage divider circuit. A PIC microcontroller needs a supply voltage of 5 volts in order to activate. A voltage divider is used to sense voltage higher than 5 volts. The resistor value of the voltage divider should be chosen in such a way that it causes a lower loss to the system, and isolates the voltage source from the PIC microcontroller. Figure 6.26 shows a voltage divider circuit.

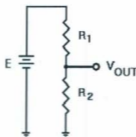


Figure 6.26 Voltage Divider Circuit

A larger value of R_2 compared to R_1 gives a larger output voltage. If the microcontroller input resistance is less than R_2 , it would diminish the output voltage, demanding more current and power from the source. But, a microcontroller has an input resistance in the mega ohm range, which is parallel to R_2 . R_2 is small enough to lessen the possibility of error. A calibration factor has been used to read the voltage. R_1 is $3k\Omega$ and R_2 is $1k\Omega$. The output voltage for the following voltage divider in Figure 6.26 is:

$$V_{out} = [R_2 / (R_1 + R_2)] E \quad (6.43)$$

6.10 Current Sensor

Current sensors are used to sense the flow of the current through a wire. It can sense either AC or DC. Some of these sense current by measuring the drop across a resistor on the current path. In this work, a current sensor Allegro ACS713 has been used. This sensor senses DC currents, and consists of a precise, low-offset, linear Hall sensor circuit with a copper conduction path. Figure 6.27 shows the diagram of the current sensor.

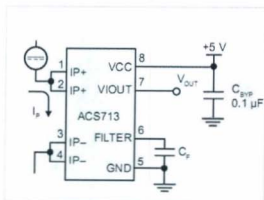


Figure 6.27 Current Sensor

Current flows through a copper conduction path from pin 1 and 2 to pin 3 and 4, where it senses the current. When current flow increases, the device has a positive slope. An internal resistor causes a very low power loss, having a value of 1.2 m Ω . It can handle five times the over current conditions because of the thickness of the copper conductor. The ACS713 is provided in a small, surface mount SOIC8 package. Conducting paths are electrically isolated from the sensing IC [77].

6.11 Energy Storage

In general, energy can be stored in many ways, such as compressed air, battery, flywheels, advanced electrochemical capacitors etc. In this work, a battery has been chosen to store energy. It is a very convenient storage device, making the system more robust. The battery is connected to the PODs, hence the PODs are self powered by the local current.

There are many types of batteries available on the market. Different batteries are suitable for different applications.

Lithium Ion batteries have a high power density but light weight. They do not have any memory effect. The charge time is about three hours and charge efficiency is 97 to 99 percent. In some cases, battery temperature rises 5°C when fully charged. For this reason it is better not to charge fully.

A Nickel Cadmium (Ni-Cd) type battery has very low internal resistance with high rate charge and flat discharge characteristics. This battery can handle deep charging. It has almost 1000 charge or discharge cycles with proper maintenance. Furthermore, it can tolerate high temperature ranges up to 70°C . Coulombic efficiency of a Ni-Cd battery is more than 75% in the first charge, but over time it slowly reduces to 50%. They are susceptible to the memory effect, so they need to be fully discharged periodically and are prone to damage by overcharging. It is economically priced per cycle.

A Nickel- Metal Hybrid contains only mild toxins, so it is environmentally friendly. It has 30 to 40 percent more capacity compared to Ni-CD and it is also less prone to the memory effect than Ni-Cd. Deep discharging reduces its life span, and it generates heat in

cases of fast charging and loading. This battery does self discharge. Temperature degrades its performance, so it should be placed in a cool location at a 40 percent state of charge.

A Lead Acid battery has a lower cost per watt-hour. This battery has a coulombic efficiency of 85%, a high specific power, and a low self discharge. But, it has a poor weight-to-energy ratio and has an environmental impact. It takes a long time to charge and should be stored in a charged condition. Both over charging or under charging reduce its life span. Its energy efficiency is about 70%.

6.12 Conclusion

This chapter discusses the steps needed to convert mechanical energy to electrical energy. A generator with a high output rating at a very low rpm would be suitable for this system. An MPPT controller works to get maximum output from the turbine. The converter output is connected with a lead acid battery. The battery supplies the pods, making them self-powered by the local current.

Chapter 7

Conclusion

7.1 Project Overview

The Ocean Network Seafloor Instrumentation (ONSFI) Project is a multidisciplinary research and development project that aims to design, fabricate and validate a proof-of-concept seafloor array of wireless marine sensors for use in monitoring seabed processes. The sensor pods, known as Seaformatics, will be powered by ocean bottom currents and will be able to communicate with each other and to the Internet through surface master units to facilitate observation of the ocean floor from the shore.

The ONSFI Project has worked with drag type devices and hybrid turbines in previous commissions. In this work, the marine current energy conversion system (MCECS) has been focused on a twisted Savonius turbine. Different analyses have been carried out to explore the twisted Savonius turbine based MCECS throughout this research work. In this thesis, a Savonius rotor has been designed with different twist angles. Experimental testing of the turbine has been performed for the 180 degree twisted Savonius vertical axis turbine. One of the main challenges was to design the twisted Savonius. Conventional Savonius turbines can be built just by employing two semi circular buckets. But, the twisted Savonius has a complex helical geometry. The prototype of the turbine was built by Seacraft International Limited. A twisted Savonius rotor emulator has been implemented to test a dc-dc converter, which includes a low cost Maximum Power point

Tracking Algorithm. The MPPT algorithm tracks the maximum power point based on the perturbation and observation method to charge the battery.

7.2 Research Contribution

The research contributions are:

- The Savonius turbine has been designed with 180^0 and quarter pitch twist along its vertical axis.
- Simulations have been done in the CFD software package Flow-3D, to determine the Power coefficient vs TSR curve for the 180^0 twisted Savonius turbine, with and without overlap ratio.
- Power coefficient vs TSR characteristics of the 180^0 twisted Savonius turbine have been explored for different axes of rotation.
- A quarter pitch twisted Savonius turbine has been simulated to establish the Power coefficient vs TSR characteristics.
- A 180^0 twisted Savonius turbine prototype has been experimentally tested in the Flume tank, as well as in the wind tunnel. Simulation results have been verified with experimental results.

- A low cost, low power microcontroller based MPPT algorithm has been developed to work on the boost converter, which has been tested with a twisted Savonius marine current emulator.

7.3 Future Work

This research work develops a marine current energy conversion system. But, this total system still needs some future development. Some suggested works are:

- Additional data on locations where the pods would be deployed is required. Depending upon the location data, changes could be made in the design of the turbine, as well as the system.
- Development is required for mounting the turbine on the ocean floor.
- In future, turbines with different twist angles like 45° , 120° , 270° and so on can be simulated to find out their characteristic curves in order to determine the best one.
- In future, effects of changing overlap ratio, aspect ratio, and the circular pattern of blades could be analyzed.
- A better permanent magnet generator has to be designed and developed to be compatible with this type of turbine. A PMG should have a better output at a very low angular speed. Depending upon generator characteristics, the decision must be made to implement either direct drive or geared coupling.

- A better dc-dc converter could be built with more efficiency and with better filters.
- A better control system can be developed to track the maximum power point instantaneously, and maintain the maximum point with the least oscillation.
- Switching loss in the converter should be considered.
- A better battery could be developed that can store the marine current energy very efficiently.

The whole system should be in a single box other than the turbine. The box must be water tight. The PMG would be coupled with the turbine, and power would be supplied to the PODs from that box. Finally, scaling laws, developed in earlier work, could be used to scale the power generated by the turbine to grid levels. These prototypes could be deployed in currents, such as the Labrador currents, or in major rivers.

Bibliography

- [1] Nahidul Khan, Michael Hinchey, Tariq Iqbal, Vlastimil Masek, 'On the Scaling Laws of Savonius Water Current Turbines', *The Journal of Ocean Technology*, Vol 5, No 2, pg. 91-99, 2010
- [2] World Energy Council, *Survey of Energy Resources 2004*
- [3] Mukund R. Patel (1999), *Wind and Solar Power System*, Publisher: Boca Raton: CRC Press
- [4] European Environment Agency (n.d.). Retrieved from <http://www.eea.europa.eu>
- [5] Caribbean Information Platform On Renewable Energy (CIPORE), (n.d.) Retrieved from <http://cipore.org>
- [6] F.L. Ponta ,P.M. Jacovkis, Marine-current power generation by diffuser-augmented floating hydro-turbines, *Renewable Energy* 33 (2008) 665–673
- [7] Ocean Energy Council (n.d.), Retrieved from www.oceanenergycouncil.com
- [8] Technology White Paper on Ocean Current Energy Potential on the U.S. Outer Continental Shelf, Minerals Management Service, Renewable Energy and Alternate Use Program, U.S. Department of the Interior, May 2006
- [9] National Aeronautics and Space Administration (n.d.). Retrieved from www.grc.nasa.gov
- [10] Ion Paraschivoiu, *Wind Turbine Design with Emphasis on Darrieus Concept*, Polytechnic International Press, June 2002
- [11] JAMES F. PRICE, ROBERT A. WELLER, REBECCA R. SCHUDLICH, 1987, *Wind-Driven Ocean Currents and Ekman Transport*, Science, Vol. 238
- [12] D. Pugh, *Changing Sea Level effects of tides weather and Climate* : Cambridge University Press, 2004
- [13] The Maury Project, American Meteorological Society (n.d.)
- [14] Charles B. Officer (1976), *Physical Oceanography of Estuaries (and Associated Coastal Waters)*, A Wiley -Interscience Publication

- [15] Sandström, J.W., Dynamische Versuche mit Meerwasser. *Annalen der Hydrographie und Maritimen Meteorologie*, 1908. 36: p. 6-23.
- [16] Bryan, F., Parameter sensitivity of primitive equation ocean general circulation models. *Journal of Physical Oceanography*, 1987. 17: p. 970-985.
- [17] Wunsch, C., Moon, tides and climate. *Nature*, 2000. 405: p. 743-744.
- [18] Robinson, A. and H. Stommel, The oceanic thermocline and the associated thermohaline circulation. *Tellus*, 1959. 11(3): p. 295-308.
- [19] Rahmstorf, S., Risk of sea-change in the Atlantic. *Nature*, 1997. 388: p. 825-826.
- [20] Roemmich, D.H. and C. Wunsch, Two transatlantic sections: Meridional circulation and heat flux in the subtropical North Atlantic Ocean. *Deep Sea Research*, 1985. 32: p. 619-664.
- [21] Ganachaud, A. and C. Wunsch, Improved estimates of global ocean circulation, heat transport and mixing from hydrographic data. *Nature*, 2000. 408: p. 453-457.
- [22] The American Practical Navigator and Epitome of Navigation Originally by Nathaniel Bowditch, LL.D (n.d.)
- [23] Lemonis, G. and J.C. Cutler, Wave and Tidal Energy Conversion, in *Encyclopedia of Energy*. 2004, Elsevier: New York. p. 385-396.
- [24] Bahaj, A.S., W.M.J. Batten, and G. McCann, Experimental Verifications of Numerical Predictions for the Hydrodynamic Performance of Horizontal Axis Marine Current Turbines. *Renewable Energy*, 2007. 32(15): p. 2479-2490.
- [25] Camporeale, S.M. and V. Magi, Streamtube Model for Analysis of Vertical Axis Variable Pitch Turbine for Marine Currents Energy Conversion. *Energy Conversion and Management*, 2000. 41(16): p. 1811-1827.
- [26] Kiho, S., M. Shiono, and K. Suzuki, The Power Generation from Tidal Currents by Darrieus Turbine. *Renewable Energy*, 1996. 9(1-4): p. 1242-1245.
- [27] M. J. Khan, M.T.Iqbal, J. E. Quaicoe, A Technology Review and Simulation Based Performance Analysis of River Current Turbine Systems. *IEEE CCECE/CCGEI*, 2006.
- [28] David, R., R. Colin, and H. Adam, *Application Areas - Offshore Processing*, in *Process Intensification*. 2008, Butterworth-Heinemann: Oxford. p. 265-286.

- [29] Owen, A. and M.L. Trevor, Tidal Current Energy: Origins and Challenges, in Future Energy. 2008, Elsevier: Oxford. p. 111-128.
- [30] Seagen (n.d.). Retrieved from <http://www.seageneration.co.uk>
- [31] Ocean Flow Energy Ltd. Development Status. 2008 Retrieved from: <http://www.oceanflowenergy.com>
- [32] Verdant Power Ltd. Verdant Power's Free Flow Turbines. 2008 Retrieved from: <http://www.verdantpower.com>
- [33] Pulse Generation Ltd. Hydrofoils or Turbines. 2008 Retrieved from: <http://www.pulsetidal.com>
- [34] OpenHydro Ltd. OpenHydro Becomes First Tidal Energy Company to Generate Electricity onto the UK National Grid. 2008. Retrieved from: www.openHydro.com.
- [35] Lunar Energy Ltd. 2008 Retrieved from: <http://www.lunarenergy.co.uk>
- [36] Blue Energy Ltd. Tidal Power. 2008. Retrieved from: www.blueenergy.com.
- [37] Aquamarine Power Ltd. Aquamarine Power Announces Contract with ABB for Neptune. 2009. Retrieved from: <http://www.aquamarinepower.com>
- [38] IHC Engineering Business Ltd. Stingray Tidal Stream Generator. 2008 Retrieved from: <http://www.engb.com>
- [39] GCK Technology Ltd. The Gorlov Helical Turbine. 2008. Retrieved from: <http://www.gcktechnology.com>
- [40] Atlantis Resources Corporation Ltd. Nereus and Solon Tidal Turbines. 2008 Retrieved from: <http://www.atlantisresourcescorporation.com>
- [41] C. P. Kothandaraman, R. Rudramoorthy, 2007, Fluid Mechanics and Machinery, Second Edition, New Age International Publishers
- [42] Merle Potter, David C. Wiggert, Ph. D, (2008), Schaum's Outline Fluid Mechanics, Publisher: McGRAW-HILL
- [43] Dr. Michael Hinchey Lecture notes on Fluid Mechanics (July, 2011), Memorial University of Newfoundland

[44] A. S. Grinspan, P. Suresh Kumar, U. K. Saha, P. Mahanta, D. V. Ratna Rao and G. Veda Bhanu, "Design, Development and Testing of Savonius Wind Turbine Rotor with Twisted Blades" Proceedings of 28th National Conference on Fluid Mechanics and Fluid Power (2001), pp. 428-431

[45] Savonius SJ. The S-rotor and its applications. *Mech. Eng*1931; 53:333-8.

[46] Manwell JF, McGowan JG, Rogers AL. Wind energy explained : theory, design and application. England : John Wiley; 2002.

[47] J. F. Manwell, J.G. McGowan, A. L. Rogers, Wind Energy Explained: Theory, Design and Application, Second Edition, 2010, Wiley-IEEE Press

[48] M. A. Kamoji, S.B. Kedar, S.V. Prabhu, 'Performance test on helical Savonius rotors', Elsevier, Renewable Energy 34 521-529, 2009

[49] Fujisawa N, Gotoh F. Experimental study on the aerodynamic performance of a Savonius rotor. *J Sol Energy Eng Trans ASME* 1994; 116:148-52.

[50] Kamoji MA, Prabhu SV, Kedare SB. Experimental investigations on the performance of conventional Savonius rotor under static and dynamic conditions. In: 33rd National and 3rd international conference on fluid mechanics and fluid power. Research Publishing Services; December 2006.

[51] Modi VJ, Fernando MS UK. On the performance of the Savonius wind turbine. *J Sol Energy Eng* 1989; 111:71-81.

[52] U. K. Saha, S. Thotla, D. Maity. Optimum design configuration of Savonius rotor through wind tunnel experiments. *Journal of Wind Engineering and Industrial Aerodynamics* 96 (2008) 1359-1375

[53] Silke Schwartz, kimono Argyriadis, Certification of Ocean Current Turbines (n.d.)

[54] Md. Jahangir Alam, Master of Engineering Thesis (2009), Design and Development of a Marine Current Energy Conversion System using Hybrid Vertical Axis Turbine, Memorial University of Newfoundland

[55] Md.Nahidul Islam Khan, M.Tariq Iqbal, Michael Hinchey, and Vlastimil Masek," Performance of Savonius Rotor as a Water Current Turbine" Maritime and Port Security, Vol. 4 No. 2, 2009

[56] <http://www.ansys.com> (n.d.)

- [57] ANSYS FLUENT 12.0 Getting Started Guide
- [58] <http://www.flow3d.com> (n.d.)
- [59] Flow 3D User Manual
- [60] Nahidul Khan, Master of Engineering Thesis (2008), 'A Micro Seafloor Marine Current Energy Conversion System' Memorial University of Newfoundland
- [61] Spooner, E., Gordon, P., Bumby, J. R., and French, C. D. Lightweight ironless-stator PM generators for direct drive wind turbines. IEE Proc. Electr. Power Appl., 2005, 152(1), 17– 26.
- [62] Bauer, P., de Haan, S. W. H., Meyl, C. R., and Pierik, J. T. G. Evaluation of electrical systems for offshore wind farms. Conference Record of the Industry Applications Conference, Rome, Italy, 8– 12 October 2000, vol. 3, pp. 1416– 1423
- [63] Chen, J., Nayar, C. V., and Xu, L. Design and finite element analysis of an outer rotor permanent magnet generators for directly coupled wind turbines. IEEE Trans. Magn., 2000, 36(5), 3802–3809 Grauers, A. Efficiency of three wind energy generator systems. IEEE Trans. Energy convers., 1996, 11(3), 650–657.
- [64] Swedish Utility Corporation. Follow up of wind power plants. Report, available in Swedish at <http://www.elforsk.se/>, 2006-07-21, 2001
- [65] M Leijon, K Nilsson, "Direct electric energy conversion system for energy conversion from marine currents." Proceedings of the Institution of Mechanical Engineers, Part A: Journal of Power and Energy 2007 221: 201 DOI: 10.1243/09576509JPE303
- [66] K. E. Hallenius, Elektriska maskiner. Lund, Sweden: CWK Gleerup Bokforlag. 1972
- [67] B. L. Theraja and A. K. Theraja, A text Book of Electrical Technology, Ram Nagar, New Delhi. 110055: S. Chand & Company Ltd, 2007
- [68] E. barbisi, F. Fiorillo and C. Ragusa, " Predicting loss in magnetic steels under arbitrary induction waeform and with minor hysteresis loops," IEEE Transections on magnetic, Vol. 40, no 4, pp. 1810-1819, July 2004
- [69] Andreas Binder, Tobias Schneider, Permanent Magnet Synchronous Generators for regenerative energy conversion- A survey (n.d.)

- [70] Rajveer Mittal, K.S.Sandu and D.K.Jain, 'Battery Energy Storage System for Variable Speed Driven PMSG for Wind Energy Conversion System' International Journal of Innovation, Management and Technology, Vol. 1, No. 3, August 2010, ISSN: 2010-0248
- [71] Muhammad H. Rashid, Power Electronics, Circuit, Devices, and Applications, Third Edition, PEARSON Prentice hall, Upper Saddle River, NJ 07458, 2004
- [72] Ned Mohan, Tore M. Undeland, William P. Robbins, Power Electronics, Converters, Applications, and Designs, Third Edition, 2003 JOHN WILEY & SONS, INC.
- [73] Simon S. Ang, Power Switching Converters, 1995 Marcel Dekker, Inc.
- [74] Eftichios Koutroulis, Kostas Kalaitzakis, 'Development of a Microcontroller-Based, Photovoltaic Maximum Power Point Tracking Control System' IEEE Transactions on Power Electronics, Vol.16, No.1, January 2001
- [75] Eftichios Koutroulis, Kostas Kalaitzakis, 'Design of a Maximum Power Tracking System for Wind-Energy-Conversion Applications' IEEE Transactions on Industrial Electronics, Vol.53, No.2, April 2006
- [76] J. H. R. Enslin and D. B. Snyman, 'Combined Low-Cost , High-Efficient Inverter, Peak Power Tracker and Regulator for PV Applications' IEEE Transactions on Power Electronics, Vol. 6. NO. I, January 1991
- [77] <http://www.allegromicro.com> (n.d.)

Appendix A

Power Coefficient vs Tip Speed ratio of the Turbine at Flume tank

clear all;

```
D=0.1524;  
H=0.4572;  
R=D/2;  
A=H*D;  
F=(2*pi)/60;  
const=0.5*1000*A;
```

hold on

```
flume40=load('0.4.txt');  
flumetor40=flume40(:,[3]);  
flumerpm40=flume40(:,[8]);  
flumespf40=load('sp0.4.txt');  
flumesp40=flumespf40(:,[1]);  
s1=sp40.^3;  
cp40=P40./(const.*s1);  
Cp40=smooth(cp40);  
aa1=smooth(tsr40,Cp40,0.1,'rloess');  
[bb,ind]=sort(tsr40);  
plot(bb,Cp40(ind),'w','bb,aa1(ind),'k.-')
```

```
flume50=load('0.5.txt');  
flumetor50=flume50(:,[3]);  
flumerpm50=flume50(:,[8]);  
flumespf50=load('sp0.5.txt');  
flumesp50=flumespf50(:,[1]);  
s2=sp50.^3;  
cp50=P50./(const.*s2);  
Cp50=smooth(cp50);  
cc1=smooth(tsr50,Cp50,0.1,'rloess');  
[dd,ind]=sort(tsr50);  
plot(dd,Cp50(ind),'w','dd,cc1(ind),'k.-')
```

```
flume60=load('0.6.txt');  
flumetor60=flume60(:,[3]);  
flumerpm60=flume60(:,[8]);  
flumespf60=load('sp0.6.txt');  
flumesp60=flumespf60(:,[1]);  
s3=sp60.^3;
```

```
cp60=P60./(const.*s3);
Cp60=smooth(cp60);
ee1=smooth(tsr60,Cp60,0.1,'rloess');
[ff,ind]=sort(tsr60);
plot(ff,Cp60(ind),'w','ff,ee1(ind),'k.-')
```

```
flume70=load('0.7.txt');
flumetor70=flume70(:,[3]);
flumerpm70=flume70(:,[8]);
flumespf70=load('sp0.7.txt');
flumesp70=flumespf70(:,[1]);
s4=sp70.^3;
cp70=P70./(const.*s4);
Cp70=smooth(cp70);
gg1=smooth(tsr70,Cp70,0.1,'rloess');
[hh,ind]=sort(tsr70);
plot(hh,Cp70(ind),'w','hh,gg1(ind),'k.-')
```

```
flume80=load('0.8.txt');
flumetor80=flume80(:,[3]);
flumerpm80=flume80(:,[8]);
flumespf80=load('sp0.8.txt');
flumesp80=flumespf80(:,[1]);
s5=sp80.^3;
cp80=P80./(const.*s5);
Cp80=smooth(cp80);
ii1=smooth(tsr80,Cp80,0.1,'rloess');
[jj,ind]=sort(tsr80);
plot(jj,Cp80(ind),'w','jj,ii1(ind),'k.-')
```

```
flume90=load('0.9.txt');
flumetor90=flume90(:,[3]);
flumerpm90=flume90(:,[8]);
flumespf90=load('sp0.9.txt');
flumesp90=flumespf90(:,[1]);
s6=sp90.^3;
cp90=P90./(const.*s6);
Cp90=smooth(cp90);
kk1=smooth(tsr90,Cp90,0.1,'rloess');
[ll,ind]=sort(tsr90);
plot(ll,Cp90(ind),'w','ll,kk1(ind),'k.-')
```

```
flume98=load('0.98.txt');
flumetor98=flume98(:,[3]);
```

```

flumerpm98=flume98(:,[8]);
flumespf98=load('sp0.98.txt');
flumesp98=flumespf98(:,[1]);
s7=sp98.^3;
cp98=P98./(const.*s7);
Cp98=smooth(cp98);
mm1=smooth(tsr98,Cp98,0.1,'rloess');
[nn,ind]=sort(tsr98);
plot(nn,Cp98(ind),'w','nn,mm1(ind),k.-')

```

```

set(gca,'XLim',[0 1.4])
set(gca,'YLim',[0 0.2])
xlabel('Tip Speed Ratio (TSR)')
ylabel('Co-efficient of Power Cp')
title('Cp-lambda curve of the turbine')
grid

```

```

sp=[flumesp40;flumesp50;flumesp60;flumesp70;flumesp80;flumesp90;flumesp98];
rpm=[flumerpm40;flumerpm50;flumerpm60;flumerpm70;flumerpm80;flumerpm90;flumerpm98];
torque=[flumetor40;flumetor50;flumetor60;flumetor70;flumetor80;flumetor90;flumetor98];

```

```

figure
yy1=smooth(sp,rpm,0.1,'rloess');
[xx,ind]=sort(sp);
plot(xx,sp(ind),'w','xx,yy1(ind),'r.-')
set(gca,'XLim',[0.4 1])
set(gca,'YLim',[0 180])
xlabel('Current Speed in m/s')
ylabel('RPM of the Turbine')
title('Current Speed vs RPM curve of the Turbine')
grid

```

```

figure
bb1=smooth(sp,torque,0.1,'rloess');
[aa,ind]=sort(sp);
plot(aa,sp(ind),'w','aa,bb1(ind),'r.-')
set(gca,'XLim',[0.4 1])
set(gca,'YLim',[0 0.3])
grid
xlabel('Current Speed in m/s')
ylabel('Torque in N-m')
title('Torque vs Current Speed curve of the turbine')

```

```

figure
Powerthr=0.5*1000*A*0.1*(sp.^3);
jj1=smooth(sp,Power,0.1,'rloess');
[ii,ind]=sort(sp);
plot(ii,Power(ind),'w.',ii,jj1(ind),'r.-')
hold on
ll1=smooth(sp,Powerthr,0.1,'rloess');
[kk,ind]=sort(sp);
plot(kk,Powerthr(ind),'w.',kk,ll1(ind),'b+-')
xlabel('Current Speed in m/s')
ylabel('Power of Turbine in Watts')
title('Output power of turbine vs current speed')
grid

```

%Power Co efficient vs TSR curve

```

const=0.5*1000*A;
s=sp.^3;
Cp=smooth(cp);
figure
mm1=smooth(tsr,Cp,0.1,'rloess');
[nn,ind]=sort(tsr);
plot(nn,Cp(ind),'w.',nn,mm1(ind),'k.-')
set(gca,'XLim',[0 1.4])
set(gca,'YLim',[0 .16])
xlabel('Tip Speed Ratio (TSR)')
ylabel('Co-efficient of Power Cp')
title('Cp-lambda curve of the turbine')
grid

```

Maximum Power, RPM and Current Speed

clear all;

```

flume40=load('0.4.txt');
flumepower40=data40(:,[4]);
flumerpm40=data40(:,[8]);

```

```

flume45=load('0.45.txt');
flumepower45=data45(:,[4]);
flumerpm45=data45(:,[8]);

```

```
flume50=load('0.5.txt');  
flumepower50=data50(:,[4]);  
flumerpm50=data50(:,[8]);
```

```
flume55=load('0.55.txt');  
flumepower55=data55(:,[4]);  
flumerpm55=data55(:,[8]);
```

```
flume60=load('0.6.txt');  
flumepower60=data60(:,[4]);  
flumerpm60=data60(:,[8]);
```

```
flume65=load('0.65.txt');  
flumepower65=data65(:,[4]);  
flumerpm65=data65(:,[8]);
```

```
flume70=load('0.7.txt');  
flumepower70=data70(:,[4]);  
flumerpm70=data70(:,[8]);
```

```
flume75=load('0.75.txt');  
flumepower75=data75(:,[4]);  
flumerpm75=data75(:,[8]);
```

```
flume80=load('0.8.txt');  
flumepower80=data80(:,[4]);  
flumerpm80=data80(:,[8]);
```

```
flume85=load('0.85.txt');  
flumepower85=data85(:,[4]);  
flumerpm85=data85(:,[8]);
```

```
flume90=load('0.9.txt');  
flumepower90=data90(:,[4]);  
flumerpm90=data90(:,[8]);
```

```
flume95=load('0.95.txt');  
flumepower95=data95(:,[4]);  
flumerpm95=data95(:,[8]);
```

```
flume98=load('0.98.txt');  
flumepower98=data98(:,[4]);  
flumerpm98=data98(:,[8]);
```



```
max40=max(flumepower40);
max45=max(flumepower45);
max50=max(flumepower50);
max55=max(flumepower55);
max60=max(flumepower60);
max65=max(flumepower65);
max70=max(flumepower70);
max75=max(flumepower75);
max80=max(flumepower80);
max85=max(flumepower85);
max90=max(flumepower90);
max95=max(flumepower95);
max98=max(flumepower98);
```

```
maxpower=[max40 max45 max50 max55 max60 max65 max70 max75 max80 max85
max90 max95 max98];
currentspeed=[0.4 0.45 0.5 0.55 0.6 0.65 0.7 0.75 0.8 0.85 0.9 0.95 0.98];
figure;
plot(currentspeed,maxpower);
xlabel('Water Speed in m/s');
ylabel('Maximum Power in watts');
title('Maximum Power vs water speed curve');
grid
```

```
maxrpm40=max(flumerpm40);
maxrpm45=max(flumerpm45);
maxrpm50=max(flumerpm50);
maxrpm55=max(flumerpm55);
maxrpm60=max(flumerpm60);
maxrpm65=max(flumerpm65);
maxrpm70=max(flumerpm70);
maxrpm75=max(flumerpm75);
maxrpm80=max(flumerpm80);
maxrpm85=max(flumerpm85);
maxrpm90=max(flumerpm90);
maxrpm95=max(flumerpm95);
maxrpm98=max(flumerpm98);
```

```
maxrpm=[maxrpm40 maxrpm45 maxrpm50 maxrpm55 maxrpm60 maxrpm65 maxrpm70
maxrpm75 maxrpm80 maxrpm85 maxrpm90 maxrpm95 maxrpm98];
figure;
plot(maxrpm,maxpower);
xlabel('Maximum RPM of turbine');
ylabel('Maximum Power in watts');
```

```
title('Maximum RPM vs Maximum Power curve');  
grid
```

Power Coefficient vs Tips Speed ratio of the Turbine at Wind Tunnel

```
clear all;
```

```
D=0.1524;  
H=0.4572;  
R=D/2;  
A=H*D;  
F=(2*pi)/60;  
fac=0.35  
con=0.5*1*A;
```

```
wind10=load('winddata10ms.txt');  
windtor10=wind10(:,[3]);  
windrpm10=wind10(:,[8]);  
windspf10=load('10testspeed.txt');  
windsp10=windspf10(:,[1]);  
windw10=(F.*windrpm10)+fac;  
windtsr10=(windw10*D)/(2.*windsp10);  
windP10=wind10(:,[4]);
```

```
s10=windsp10.^3;  
cp10=windP10./(con.*s10);  
Cp10=smooth(cp10);  
figure  
aa1=smooth(windtsr10,Cp10,0.1,'rloess');  
[bb,ind]=sort(windtsr10);  
plot(bb,Cp10(ind),'w','bb,aa1(ind),'k.-')  
xlabel('Tip Speed Ratio (TSR)')  
ylabel('Co-efficient of Power Cp')  
title('Cp-lambda curve of the turbine at 10m/s')  
grid
```

```
wind13=load('winddata13ms.txt');  
windtor13=wind13(:,[3]);  
windrpm13=wind13(:,[8]);  
windspf13=load('13testspeed.txt');  
windsp13=windspf13(:,[1]);  
windw13=(F.*windrpm13)+fac;  
windtsr13=(windw13*D)/(2.*windsp13);  
windP13=wind13(:,[4]);
```

```
s13=windsp13.^3;
cp13=windP13./(con.*s13);
Cp13=smooth(cp13);
figure
cc1=smooth(windtsr10,Cp10,0.1,'rloess');
[dd,ind]=sort(windtsr10);
plot(dd,Cp10(ind),'w.',dd,cc1(ind),'k.-')
xlabel('Tip Speed Ratio (TSR)')
ylabel('Co-efficient of Power Cp')
title('Cp-lambda curve of the turbine at 13m/s')
grid
```

Appendix B

Flow-3D Simulations

Flow-3D version 9.4.1 has been used to do the simulations in this research work.



Figure B 1 Flow-3D version 9.4.1

Main Menu

The main menu is displayed at the very beginning of starting of Flow-3D. Figure B 2 shows the Main Menu.



Figure B 2 Main Menu

File Menu

The file menu contains the options such as new workspace, new simulation, save etc.

Figure B 3 shows File Menu.



Figure B 3 File Menu

To create a simulation a workspace has to be created, using 'New workspace' available in the file menu (Figure B 4). The name of the workspace and the directory for the following workspace can be defined.

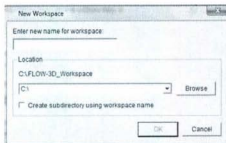


Figure B 4 New Workspace

The workspace can be saved using the option 'Save Workspace As'. Different simulation files can remain under the same workspace, having different names or the files might be in different directory. 'Open Workspace' opens the Workspace which is already created. The Workspace might be in different locations, so the directory has to be mentioned to open a certain Workspace. New simulation can be introduced using 'add new simulation'. Flow-3D simulation input file is in '.prepin' format. A new .prepin file is generated when 'add new simulation' is used. Figure B 5 shows the dialog box for New Simulation.

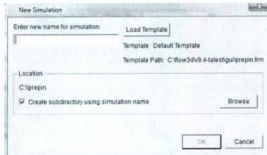


Figure B 5 New Simulation

If a simulation exists in the workspace, simulation input .prepin file can be opened by 'Add existing simulation'. There are also some other options, such as Import Existing Simulation, Add Simulation Copy, and Add Example. 'Save Simulation' saves the current working simulation in the current directory. 'Save Simulation As' saves the simulation under a different name of input file and save in a selected directory. 'Edit Simulation' opens the input file in a text editor to modify. 'Rename' can be used to define a different name of the input file. In the structure tree, there might be either one Workspace or more than one. 'Close Workspace' closes a workspace. 'Remove Simulation' removes a simulation from the workspace but does not delete the simulation from the directory. 'Exit' closes Flow-3D.

Diagnostics Menu

The Diagnostics menu is used to view diagnostics files generated by Flow-3D in Figure B 6. This is very useful for troubleshooting.

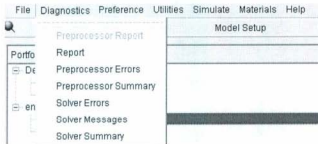


Figure B 6 Diagnostics

The number of computational cells used in a particular direction, the total number of cells in the model (including boundary cells), open areas on boundaries, amount of fluid initially in the model, etc. can be determined from preprocessor report. It has some other source of information such as Report, Preprocessor Errors, Preprocessor Summary, Solver Errors, Solver Messages, and Solver Summary. At the beginning of the simulation, Solver Messages gives some important information like the memory requirement for the simulation results. Figure B 7 shows the Solver report for one of the simulations of the twisted Savonius rotor. Simulation generates an output file of 8GB. It also shows the starting time of the simulation and some other information, as well.

```

program title : FLOW-3D
program version : hydr3d: version 9.4.1 win32-ifl 2010
version id : double
DOUBLE precision version
process identification number for this job= 1

Job name: eifd
problem date: 09/10/2010
problem time: 17:49:0400

Title

*** estimated uncompressed solver output file size (flagrf): 0 gb ***

*** running parallel code on 2 processors ***

***
restart and spatial data available at t= 0.00000E+00
***

t          cycle  iter  dstatbl/code  delt      eps1      cpu      clock
----          ---  ---  -----  ---      ---      ---      ---
0.00E+00      0      0  5.81E-04/cy  5.81E-04  -1.0E+00  2.5E+00  17:49:09

```

Figure B 7 Solver Report

'Solver Summary' is used to view detailed information about the simulation, such as the number of voids in the simulation at a specified time, the computed stability criteria, at what cells the criteria are a minimum, etc. which are important to study simulation efficiency.

Preference Menu

The options under the preference menu specify certain preferences for running FLOW-3D. It has the options Sub-tab Color, Default Workspace Location, Runtime Defaults, Add Existing Simulation starts in Workspace, Auto Save Before Simulating, and Switching Between Simulations (Figure B 8).



Figure B 8 Preference Menu

In the simulations of the twisted Savonius turbine the double precision version has been used, which is done from Runtime Defaults (Figure B 9).

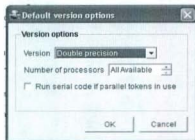


Figure B 9 Runtime Defaults

Utilities Menu

The utilities menu is used to access certain programs like Uncompressed and Auto update Imtools. Figure B 10 shows the utilities menu.

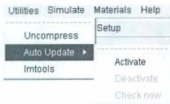


Figure B 10 Utilities Menu

Simulate Menu

Either the preprocessor or the solver for Flow-3D can be launched in the Simulate menu.

Figure B 11 shows different options of the Simulate menu.

Simulate	Materials	Help
Preprocess Simulation		Ctrl+R, Ctrl+P
Run Simulation		Ctrl+R, Ctrl+S
Simulate Workspace		Ctrl+R, Ctrl+W
Simulate Portfolio		
Terminate Simulation ...		Ctrl+T
Clear Simulation List		
Set Max Simultaneous Simulations (1) ...		

Figure B 11 Simulate Menu

Preprocess Simulation launches the Flow-3D preprocessor for a selected simulation. Run Simulation starts the simulation of the selected simulation file, launching Flow-3D solver. If a simulation runs, this option remains inactive and 'Terminate Simulation' is activated (Figure B 11). Simulate Workspace is used to launch the Flow-3D solver for all simulation input files in a certain Workspace. Simulate Portfolio is used to launch the Flow-3D solver for all simulation files in all Workspaces. Multiple simulations can be run either at the same time or one after another in a single session of Flow-3D, and then, they are added in a queue drop down box in the Navigator tab. Thus, many simulations can exist in the list that can be cleared by 'Clear Simulation List'. In this case, the running simulation remains undisturbed. The maximum number of simultaneous simulations for

users with multi-processor computers and license can be set by using 'Set Max Simultaneous Simulations'.

Navigator

If Navigator is pressed, the following window (Figure B 12) appears. The portfolio shows the tree in the left side of the window. It shows that there are two Workspaces and in total four simulations. Every simulation has its own '.prepin' file.

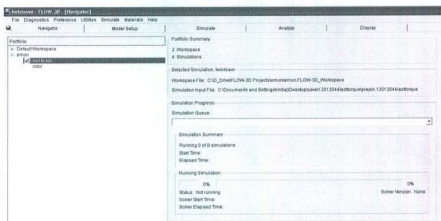


Figure B 12 Navigator

The Portfolio summary gives information about total Workspaces and simulation in the portfolio tree. Figure B 12 shows the Workspace directory, C:\D_Drive\Flow-3D Projects\emom\emom.Flow-3D_Workspace, and the simulation directory as C:\Documents and Settings\Intiaj\Desktop\save\prepin.12012044lasttorque.

Model Setup

To create a simulation, different parameters are setup under the tab Model Setup. Modification on the existing simulations can also be done. It has eight sub-tabs.

General

The General tab under Model Setup is shown in Figure B 13 for the simulation of the twisted Savonius.

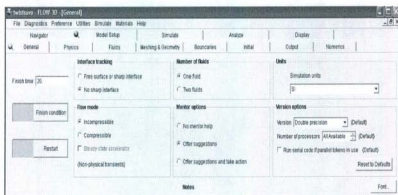


Figure B 13 General Tab

The real world time to observe the behavior of the turbine, is assigned in 'General'. The simulation of the twisted Savonius is done for 20 seconds. No sharp interface has been chosen from Interface tracking. Incompressible fluid has been assumed for all the simulations. The turbine is supposed to be deployed under the Atlantic Ocean, so, one fluid has been considered. In the mentor options 'Offer suggestions' has been chosen. SI unit system has been taken for all the simulations. Double precision version has been activated.

Physics

Many options are shown in the Physics tab (Figure B 14). Among them Gravity, Moving and deforming objects, and Viscosity and turbulence has been activated.

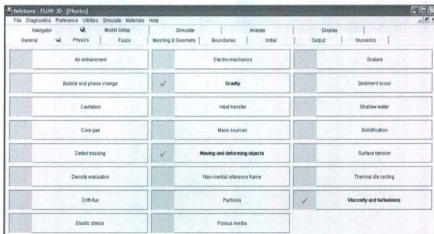


Figure B 14 Physics Tab

Gravity

The turbine is placed along z direction. In the gravity vector -9.81 m/s^2 has been chosen for the gravity component in z direction (Figure B 15).

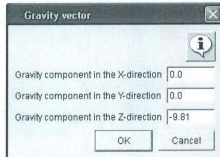


Figure B 15 Gravity Vector

Moving and Deforming Objects

The Moving object model has been activated using this option. Implicit fluid coupling has been used (Figure B 16).

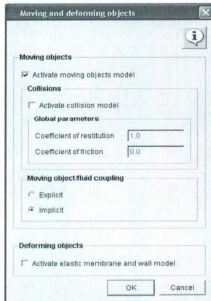


Figure B 16 Moving and Deforming Objects

Viscosity and Turbulence

Viscous flow has been considered. As this work deals with under water environment, flow has been considered as turbulent. No slip or partial slip has been considered for wall shear boundary conditions. This is a renormalized group model and maximum turbulent mixing length is dynamically computed. Figure B 17 shows the box for viscosity and turbulence for the turbine simulation.

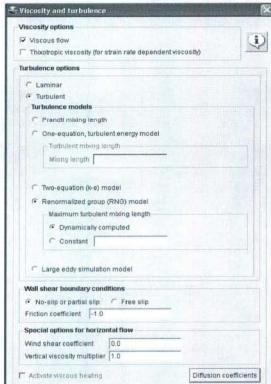


Figure B 17 Viscosity and Turbulence

Fluids

'Fluids' basically deals with the fluid properties that can be used for the simulation. In this work only one fluid has been used.

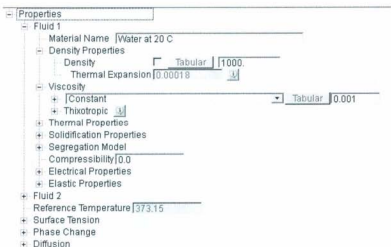


Figure B 18 Fluids

Meshing and Geometry

The computational mesh can be created or modified in this sub tab. Moreover, specifying certain quantities and properties (thermal conductivities, heat transfer coefficients, and moving object properties) can be fixed up in this sub-tab. Figure B 19 shows the window for the meshing geometry.

The Meshing and Geometry sub-tab has a tree structure on the left side, providing a considerable amount of information about the components and the mesh blocks. Figure B 22 shows the upper portion of the tree structure.

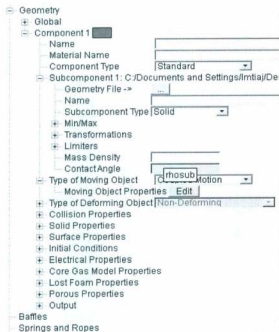


Figure B 22 Meshing and Geometry Tree Structure (Part 1)

The very first option of this part is 'global'. This is basically the dimension of the turbine or component that is imported in the Flow-3D in the three dimensional co-ordinate. The .STL of the twisted Savonius has been imported in Flow-3D using the option Geometry File under Subcomponent 1. Figure B 23 shows the Moving object properties.

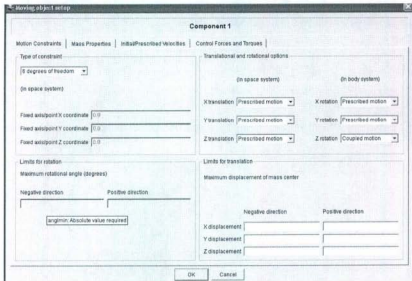


Figure B 23 Moving object properties

The moving objects properties include four more tabs. First of them is 'Motion Constrain'. For the type of constrain, 6 degree of freedom has been used. All the motions are prescribed motions, except the z rotation is a Coupled motion.

'Initial and prescribed velocity' and 'Mass Properties' are other tabs. The last one is 'Control Forces and Torques'. It gives the option to impose the torque on the moving body. A set of control torque was imposed on the turbine using this option. Figure B 24 shows the Control Forces and Torque.

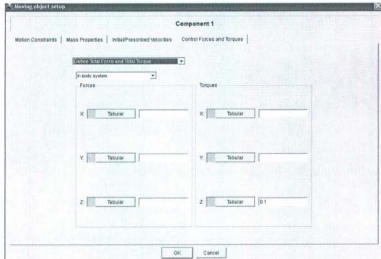


Figure B 24 Control Forces and Torque

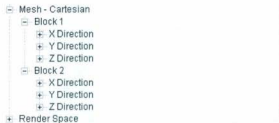


Figure B 25 Meshing and Geometry Tree Structure (Part 2)

Figure B 25 shows rest of the tree in Meshing and Geometry. Two mesh blocks have been used for the simulation. Under the Mesh- Cartesian, two mesh blocks can be finalized. It allows defining number of cells, starting point, and ending point of the mesh block in all the x, y, and z directions. Turbine has been imported in block 1. Figure B 26 shows the turbine in the mesh.

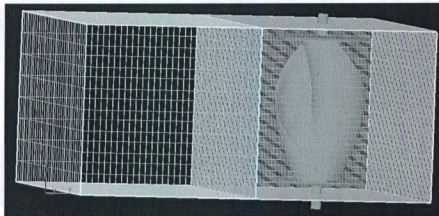


Figure B 26 Turbine in the mesh

The orientation can be changed to x-y, x-z, or y-z views by using the appropriate icons in the Toolbar (Figure B 27).



Figure B 27 Graphic Toolbar

If the mouse cursor is positioned on the surface of the object, 'Probe' shows the position of the cursor in the co-ordinate system (Figure B 28).

Probe: X: 0.0 Y: 0.0 Z: 0.0

Figure B 28 Probe

Boundaries

The desired boundary condition can be fixed up from the sub tab 'Boundaries'. In Flow-3D, each boundary of the computational domain has an associated boundary condition. Figure B 29 shows the boundary conditions used for the simulations.

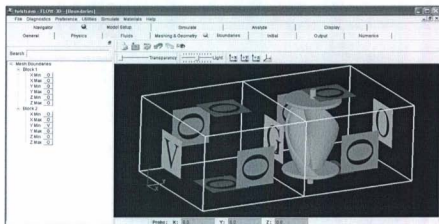


Figure B 29 Boundary Conditions

To assign each of the boundary conditions, every boundary has a different dialog box in Flow 3D. Figure B 30 shows one of the dialog boxes for the out flow.

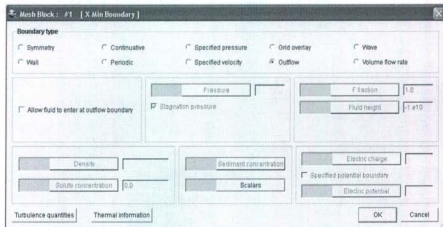


Figure B 30 Dialog box to fix up Boundary Condition

Initial

Fluid and void initial conditions can be corrected from 'Initial' along with the constant pressures, velocities, and temperatures. This sub tab also gives the option to assign u, v, and w velocity. This tab also deals with some other initial properties such as temperature, fluid rotation, etc. For this work only, the v velocity has been assigned, and there is hydrostatic pressure in z direction only, as shown in the dialog box in Figure B 31.

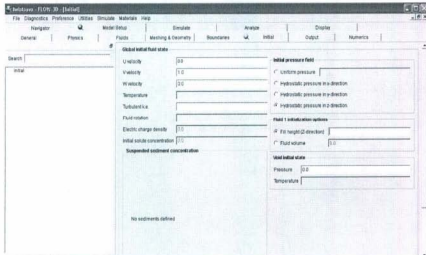


Figure B 31 Initial dialog box

Output

The frequency of plot output and animation output can be determined from 'Output'. For this work, a time interval of 0.1 second has been used in Figure B 32.

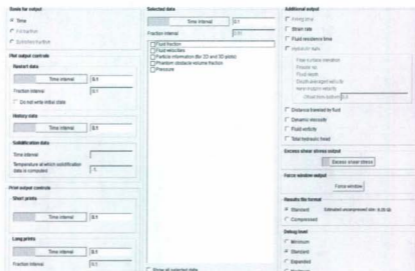


Figure B 32 Output subtab

Numerics

Numerics sub tab has been used to correct the following options in Figure B 33. For this simulation first order momentum advection was used. Solve momentum and continuity equation has been activated for the fluid flow solver option. Time step size is controlled by Stability and Convergence.

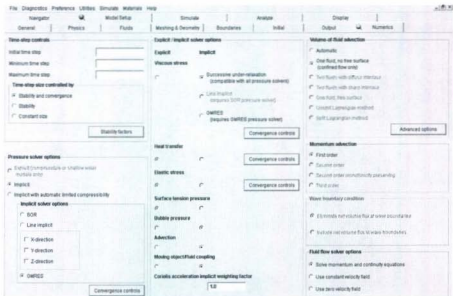


Figure B 33 Numerics subtab

Simulate

Plots for some of the parameters are found in 'Simulate'. Figure B 34 is the simulation result of the twisted Savonius rotor imposing 0.1 N-m torque.

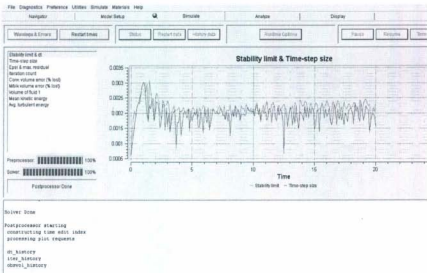


Figure B 34 Simulate Tab

Analyze

Once the simulation is done, the result is analyzed by the tab 'Analyze', as shown in Figure B 35. In this tab, results can be customized according to the requirement. One-Dimensional plots, display a computed value in the selected direction, along a row of cells through the mesh. For the two dimensional analysis, different combinations can be chosen to observe the output results. The simulation results can also be analyzed three dimensionally. There are different subtabs named probe, 1D, 2D, and 3D as shown in Figure B 35. The result can be visualized through rendering it. Flow-3D can generate text output of the simulation too. Text Output generates data in text form in a data window.

The data can be inspected in the window and can be saved as an ASCII file. Flow 3D also generates a file named Neutral file, which can be saved as an ASCII file.

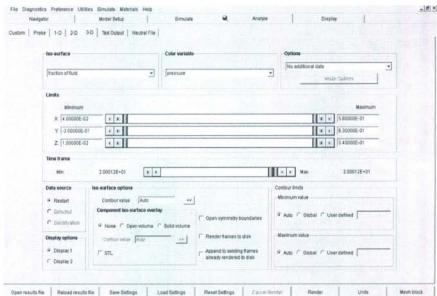


Figure B 35 Analyze Tab

Display Tab

The Display tab basically shows the results after rendering in the Analyze tab. The graphical output generated by the postprocessor is shown in the Canvas Window. The Control Panel of the display tab helps to change a variety of plot settings. There is a Menu bar and Toolbar both for 2D and 3D format display. There is a probe data box in 3D display. If the mouse cursor is positioned on the object surface, the Probe Data Box will display the position in the coordinate system. Figure B 36 shows the window for 3D display.

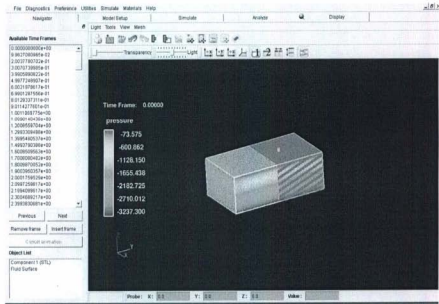


Figure B 36 Display windows for 3D format

Appendix C

Continuous Mode

In mode 1 of continuous mode, MOSFET M is in ON state, which means switch is closed. M is turned ON at $t = 0$ and remains on the same state till $t = t_{on}$. Diode D is reverse biased. Figure C 1 shows the circuit diagram for mode 1 operation.

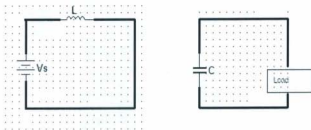


Figure C 1 Boost converter equivalent circuit for Mode 1 operation

In the equivalent circuit in Figure C 1, source current I_s and inductor current is same $I_s = I_L$. Capacitor current is I_c and load current is $i_o(t)$ which is the average output current I_o . In mode 1, output voltage and current are due to the capacitor. The capacitor value is chosen carefully so that it can supply the output current during the t_{on} period. Current from the supply flows through the inductor; inductor current rises linearly, and energy is stored in the inductor. Inductor current increases linearly from I_1 to I_2 in a period of t_{on} , so

$$L \frac{di_L(t)}{dt} = V_s$$

$$\text{Or, } V_s = L \frac{I_2 - I_1}{t_{on}} = L \frac{\Delta I}{t_{on}} \quad (\text{C.1})$$

t_{on} can be expressed as equation C.2.

$$t_{on} = \frac{L \Delta I}{V_s} \quad (C.2)$$

During $0 \leq t \leq t_{on}$ period energy stored in the inductor is

$$E = 0.5 L(\Delta I)^2 = V_s^2 t_{on}^2 / 2L \quad (C.3)$$

In mode 2, MOSFET is turned OFF at time $t=t_{on}$. Inductor cannot change current instantaneously through it. Polarity of the inductor voltage changes to maintain a constant current. Diode D is on forward biased so conducting the current from the supply. Current flows through the inductor, diode, C, and load and back to the source. In the mean time, inductor current keeps falling until next cycle comes. In this mode, inductor delivers stored energy to charge the capacitor through the diode to a higher voltage than input voltage V_s . Capacitor supplies the current to the load and charge is drained to the load during t_{on} period. Figure C 2 shows the operation of mode 2.

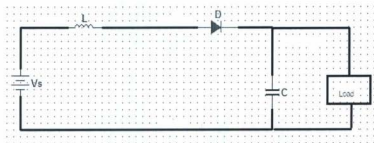


Figure C 2 Boost converter equivalent circuit for Mode 1 operation

During this period of t_{off} inductor current falls from I_2 to I_1 , and voltage across the inductor is $V_s - V_D$.

$$V_s - V_a = L \frac{I_2 - I_1}{t_{off}}$$

$$\text{Or, } V_a - V_s = L \frac{\Delta I}{t_{off}} \quad (\text{C.3})$$

t_{off} can be expressed as

$$t_{off} = \frac{L\Delta I}{V_a - V_s} \quad (\text{C.4})$$

In mode 1 inductor current rises from I_1 to I_2 and in mode 2 inductor current falls from I_2 to I_1 . So, inductor ripple current is ΔI . For a steady state operation of the converter peak to peak ripple current of the inductor is the same during t_{on} and t_{off} period. So,

$$\Delta I = \frac{V_s t_{on}}{L} = \frac{(V_a - V_s) t_{off}}{L} \quad (\text{C.5})$$

$t_{on} = DT$ and $t_{off} = (1-D)T$. Substituting these values into equation C.5.

$$V_s DT = (V_a - V_s)(1-D)T = V_a (1-D)T - V_s(1-D)T$$

Simplification gives

$$V_s = V_a (1-D) \quad (\text{C.6a})$$

$$\text{Or, } V_a = V_s / (1-D) \quad (\text{C.6b})$$

Average output voltage of the converter is inversely proportional to $(1-D)$. Equation C.6a and C.6b show the relation between input voltage and average output voltage. But, duty cycle D can never be equal to unity. If D is zero that means the output voltage is equal to the input voltage. As the duty cycle tends to increase to unity output, voltage tends to increase. So, V_o is always greater than the input voltage, which means it always steps up the voltage. For a lossless converter

$$V_s I_s = V_a I_a = V_s I_o / (1-D) \quad (\text{C.7})$$

Input current to the converter can be expressed as

$$I_s = I_a / (1-D) \quad (C.8)$$

Average output current is always less than that of the input current. So, for boost converter average output voltage is higher than the input voltage and output average current is always less than the input current.

Switching period T can be expressed as

$$T = 1/f_s = t_{on} + t_{off} = \frac{L \Delta I}{V_g} + \frac{L \Delta I}{V_g - V_a} = \frac{V_a L \Delta I}{(V_g - V_a) V_g} \quad (C.9)$$

Where, f_s is the switching frequency. Peak to peak ripple current is

$$\Delta I = \frac{V_g [\frac{V_g}{1-D} - V_g]}{L f_s V_a} = V_a D / f_s L \quad (C.10)$$

The magnitude of inductor ripple current is proportional to supply voltage and duty ratio and inversely proportional to switching frequency and inductance. When M is ON, capacitor supplies the load current. So, the average output current is equal to the capacitance current for this period. When the switch is OFF, capacitor is charged. Capacitor charging current falls linearly from $I_2 - I_a$ to $I_1 - I_a$. In steady state, average capacitor charging current time product must be equal as average capacitor discharging current time product. So, there is also ripple in the capacitor voltage because voltage across a capacitor cannot change instantly. When switch is ON then average output current comes from the capacitor. So, voltage ripple

$$\Delta v_c = v_c - v_c(0) = \frac{1}{C} \int_0^{t_{on}} I_a dt = \frac{I_a t_{on}}{C} \quad (C.11)$$

From equation C.6b

$$V_a = V_g / (1-D) = V_g T / (T-DT) = V_g T / T - t_{on}$$

$$\text{Or, } T-t_{\text{on}} = V_s T / V_a \quad (\text{C.12})$$

$$\text{So, } t_{\text{on}} = (V_a - V_s) / f_s V_a \quad (\text{C.13})$$

$$\text{Voltage ripple } \Delta V_c = \frac{I_a (V_a - V_s)}{f_s C V_s (1-D)} = \frac{I_a D}{f_s C} \quad (\text{C.14})$$

The ripple voltage is proportional to the average output current and duty ratio and inversely proportional to switching frequency and capacitance.

Discontinuous Mode

If the inductor current falls to zero before the next cycle comes, the operation of the boost converter is said Discontinuous Mode.

Assuming input power of the boost converter is equal to output power.

$$V_s I_a = V_a^2 / R$$

Average inductor current is

$$I_L = \Delta I / 2 = \frac{V_s D}{2 f_s L} \quad (\text{C.15})$$

Input current I is equal to inductor current I_L

$$V_s \frac{V_s D}{2 f_s L} = V_a^2 / R \quad (\text{C.16})$$

$$\text{Critical inductor } L_c = RD(1-D)^2 / 2f_s \quad (\text{C.17})$$

If the nominal resistance is greater than critical resistance, boost converter works in discontinuous mode.

$$R_c = R_{\text{nom}} / D(1-D)^2 \quad (\text{C.18})$$

Where $R_{\text{nom}} = 2f_s L$ which is a design parameter.

Average voltage across the inductor during DT interval, is V_s and during D_2T interval is $V_a - V_s$. So,

$$V_s D - (V_a - V_s) D_2 = 0 \quad (C.19)$$

Where, $D_2 = (t_2 - t_{on})/T$

Average inductor current is equal to average input current.

$$I_L = \frac{V_s D}{2f_s L} \quad (C.20)$$

$$\text{Average output current, } I_a = \frac{1}{T} \int_{t_{on}}^{t_2} I_L dt = \frac{t_2 - t_{on}}{T} I_L \quad (C.21)$$

In discontinuous mode operation, open loop voltage conversion ratio is

$$V_a/V_s = 1 + \sqrt{[1 + 4DL_c/L(1-D)^2]}/2 \quad (C.22)$$

From equation C.22, it is proved that in discontinuous mode, voltage conversion ratio increases in a higher rate with duty ratio compared to a continuous mode of operation. At the beginning of operation, a higher current compared to the steady state current flows before it reaches the steady state. Converter is designed in such a way that it can handle this. Value of the inductor should be suitable enough that it does not get saturated because of the higher inrush current at the beginning of the operation.

Appendix D

Boost Converter Design:

clear all;

fr=5000;
ripl=0.001;
n=0.8;
Vd=0.7;

gain=2.5;
vi=0.5:8:2;
vo=gain.*vi;
D=(vo-vi)./vo
t=1/f
ton=D.*t
toff=(1-D).*t

R=50;
lmin=(R./(2*f)).*D.*(1-D).*(1-D);
l=1.2*lmin;
c=D/(R.*f*ripl);

viex=load('inputvoltage.txt');
voex=load('outputvoltage.txt');
iiex=load('inputcurrent.txt');
ioex=load('outputcurrent.txt');
piex=viex.*iiex;
poex=voex.*ioex;

io=vo/R;
po=io.*vo;
di=(vi/l).*D.*t
iavg=io.*(1-D)
imax=iavg+(di/2)
imin=iavg-(di/2)
figure
plot(vi,po,'-r')
hold on
plot(viex,poex,'-r')
xlabel('Input Voltage(V)')
ylabel('Output power(W)')
title('Output Power of DC DC Converter')

```

grid
figure
plot(vo,io,'-r*')
hold on
plot(voex,ioex,'-r*')
xlabel('Output Voltage(V)')
ylabel('Output Current(A)')
title('Output Voltage and Current')
grid
figure
plot(vi,vo,'-r*')
hold on
plot(viex,voex,'-r*')
xlabel('Input Voltage(V)')
ylabel('Output Voltage(V)')
title('Output Voltage vs Input Voltage')
grid
figure
plot(vo,po,'-r*')
hold on
plot(voex,poex,'-r*')
xlabel('Output Voltage(V)')
ylabel('Output Power(W)')
title('Output Power vs Voltage')
grid
n=poex/piex
figure
plot(viex,n,'*')
xlabel('Input Voltage(V)')
ylabel('Output Power(W)')
title('Output Power vs Voltage')
grid

```

Appendix E

MPPT Algorithm

```
/*
-Start the pwm to the MOSFET at some set value
-measure the current Input
-measure the voltage of the bus
-calculate the power
-increment the turn on period of the pwm
-measure the current and bus voltage again
-calculate the new power value
-if the power has dropped, reduce the duty cycle of the pwm
-if the power has increased, increase the duty cycle of the pwm
-repeat the steps
*/
#include <16f877.h>
#DEVICE *=16 ADC=10
#use Delay(Clock=2000000)
#use rs232(baud=9600, xmit=PIN_C6, rcv=PIN_C7)
#include<lcd.c>

// initialize constants and variables

CONST long d_hill = -10;
CONST byte in_volt = 0, in_amp = 1, out_volt = 2, out_amp = 3;
float input_current, output_current, input_voltage, output_voltage;
float D=0.5,H=1.0,V=1.0,Cp=0.12,tsr=0.7,opt_w,opt_tor,cap_pow,ins_w;
float input_power=0.0, output_power=0.0,old_output_power=0.0,error;
long u_hill = 10, pwm_max, pwm=500.0,pwm_min;
long boost = 0, boost_gain;
boolean run;

// Global Variables
boolean meas_done = FALSE, once = TRUE ;
unsigned int8 loops = 0;
unsigned int32 RPM, sensor_pulses = 0;

#int_EXT
EXT_isr(){

    if(!meas_done){
```

```

    sensor_pulses++; // Sensor pulses into PIN_B0
  }
}
#endif
TIMER1_isr(){

  if(loops){
    loops--;
  }
  else if(loops==0){
    meas_done=TRUE;
  }
}

//-----
// This function is used to set the duty cycle of the PWM output. It uses the built
// in C compiler function set_pwm1_duty to set the duty cycle.
//-----

void start_measurement(){

if (once == TRUE){ // only executes once until measurement is complete.

  meas_done=FALSE;
  loops = 19; // 52.5ms * 19 = ~1000ms(997.6ms)
              // This is the measurement window time

  enable_interrupts(INT_TIMER1); // To create a measurement window
  enable_interrupts(INT_EXT); // Generate an interrupt every pulse
                               // coming from the sensor
  set_timer1(0);
  once = FALSE;
}
}

float input_channel(byte chan) {

  int i,avg_num =10;
  float avg = 0;

  set_adc_channel(chan);
  delay_us(100);
  for (i=1; i<=avg_num; ++i) {
    avg += read_adc();
  }
}

```



```

    delay_us(1000);
}
return(avg/avg_num);
}
// Input voltage,current and power

void in_power(){
input_voltage = input_channel(in_volt)*0.01955034;
input_current =((0.0262*( input_channel(in_amp))) -(2.8332));
input_power = input_current * input_voltage;
}

//Output voltage,current and power
void out_power(){
output_voltage = input_channel(out_volt)*0.01902125;
output_current=((0.0258*( input_channel(out_amp))) -(2.8332));
output_power = output_current * output_voltage;
}
void main()
{

// initialize encoder

setup_timer_1(T1_INTERNAL | T1_DIV_BY_4); //interrups every 0.0525088s
ext_int_edge(H_TO_L);
enable_interrupts(GLOBAL);

// initialize hardware

setup_port_a(ALL_ANALOG); // set up A/D channels
setup_adc(adc_clock_div_32); // start A/D clocks
setup_timer_2(T2_DIV_BY_4,249,1); // pwm frequency 5kHz
setup_ccp1(CCP_PWM); // Configure CCP1 as a PWM
pwm_max = 1000; // maximum value for PWM based on frequency
pwm_min=10;
pwm = 100; // set pwm to 85% to start
lcd_init();
output_high(PIN_C3); // set enable pin on FET driver
output_high(PIN_C0); // turn on green led
delay_ms(10); // delay to get started

for (;;) { // loop forever
start_measurement();

```

```

if (meas_done){ // only updates when measurement is complete.
  disable_interrupts(INT_EXT);
  disable_interrupts(INT_TIMER1);
  RPM = (sensor_pulses * 60)/256;
  sensor_pulses = 0;
  once = TRUE;
}

opt_w=15;
cap_pow=0.5*1000*H*D*Cp*(V*V*V);
opt_tor=cap_pow/opt_w ;
ins_w= (2*3.142*RPM)/60;

in_power();
out_power();

if (output_voltage<12){
  output_high(PIN_B1);
  output_low(PIN_B2); }

if (output_voltage>12){
  output_low(PIN_B1);
  output_high(PIN_B2); }

error=ins_w-opt_w;
if (error>0){
  pwm+=u_hill;
  set_pwm1_duty(pwm);}
if (error<0){
  pwm+=d_hill;
  set_pwm1_duty(pwm);
}
pwm=pwm;
if (pwm>=pwm_max) pwm=pwm_max;
if(pwm<=pwm_min) pwm=pwm_min;

lcd_putc('\f');
printf(lcd_putc,"input_voltage=%4.2F",input_voltage);
printf(lcd_putc,"input_current=%4.2F",input_current);
printf(lcd_putc,"output_voltage=%4.2F",output_voltage);
printf(lcd_putc,"output_current=%4.2F",output_current);

```

```
printf("%4.2F %4.2F %4.2F %4.2F %4.2F %4.2F %04lu %4.2F %04lu \n \r"  
input_voltage,input_current,input_power,output_voltage,output_current,output_power,RP  
M,ins_w,pwm);
```

```
delay_ms(1000);  
run=TRUE;  
} //end forever loop  
} //end main
```

